

# **Structural, Opto-electronic, Electrical and Photo sensing properties of Al-Li co-doped NiO and Mn doped ZnTiO<sub>3</sub>**

**M.Sc. Thesis**

By  
**Mahesh Kumar**



**DISCIPLINE OF PHYSICS**  
**INDIAN INSTITUTE OF TECHNOLOGY INDORE**  
**JUNE 2021**







# **Structural, Opto-electronic, Electrical and Photo sensing properties of Al-Li co-doped NiO and Mn doped ZnTiO<sub>3</sub>**

**A THESIS**

*Submitted in partial fulfillment of the  
requirement for the award of the degree  
of  
Master of Science*

*By*  
**Mahesh Kumar**



**DISCIPLINE OF PHYSICS  
INDIAN INSTITUTE OF  
TECHNOLOGY INDORE**

**June 2021**



## INDIAN INSTITUTE OF TECHNOLOGY INDORE

### CANDIDATE'S DECLARATION

I hereby certify that the work which is being presented in the thesis entitled **STRUCTURAL, OPTOELECTRONIC, ELECTRICAL AND PHOTSENSING PROPERTIES OF Al-Li CO-DOPED NiO AND Mn DOPED ZnTiO<sub>3</sub>** in the partial fulfillment of the requirements for the award of the degree of **MASTER OF SCIENCE** and submitted in the **DISCIPLINE OF PHYSICS, Indian Institute of Technology Indore**, is an authentic record of my own work carried out during the time period from July 2020 to June 2021 under the supervision of Dr. Somaditya Sen, Associate Professor, Indian Institute of Technology Indore.

The matter presented in this thesis has not been submitted by me for the award of any other degree of this or any other institute.

15/06/2021

**Signature of the student  
(MAHESH KUMAR)**

This is to certify that the above statement made by the candidate is correct to the best of my/our knowledge.

Signature of the Supervisor of

M.Sc. thesis (with date)

**(Dr. Somaditya Sen)**

20th June 2021

MAHESH KUMAR has successfully given his/her M.Sc. Oral Examination held on **19/06/2021**.



24-06-2021

Signature(s) of Supervisor(s) of MSc thesis Convener,  
Date:



24-06-2021

DPGC  
Date:



Signature of PSPC Member #1  
Date:

Signature of PSPC Member #2  
Date:

-----

## **ACKNOWLEDGEMENTS**

This thesis is the culmination of my journey in procuring my Master of Science (M.Sc.) degree in Physics. This journey Without you, none of this would have been possible. the constant vindication, motivation, and encouragement of some folk. Firstly, I'd like to thank the Lord our God for all things are possible only through him and nothing is without him. I'd like to express my sincere gratitude to my thesis advisors Dr. Somaditya Sen who took me under his wings and has been a continual source of encouragement and support motivation. Without him this journey would not have been possible. He has always been there with valuable ideas and guidance, always ready to lend a helping hand. Dr. Somaditya Sen has been a brilliant mentor guiding me not only in my academics but also in different walks of life. His constant support, valuable advice, constructive criticism, and extensive discussion helped me in accomplishing my M.Sc. Moreover, his principles, noble thoughts, fatherly care, and simplicity always influenced me and will always help me in becoming a good person. It has been my privilege and honor to work with him and It's been a fantastic learning opportunity for me throughout my study at IIT Indore. I'd like to express my gratitude sincerely. I am grateful to my mother and my siblings for all the sacrifices they made on my behalf. My mother has always been a source of encouragement and motivation for me, and her prayers have kept me going through all the difficult times in my life.

I take this opportunity to sincerely acknowledge Dr. Biwarup Pathak and Dr. Rajesh Kumar (PSPC) for evaluating and giving their valuable comments for improving my research work.

I want to thank the whole Science department for providing all the resources and facilities for accomplishing my M.Sc. thesis. I thank SIC facilities IIT Indore. I extend my grateful 'thank you' to the workshop and glass blowing section for helping me fabricate the in house-experimental setup.

My M.Sc. the thesis would not have been possible without the help of colleagues. I sincerely thank my lab mates Ruhul Amin, Koyal Suman Samantray,

Saniya Ayaz, Prashant Mishra, Hima MP, Rachit Dobhal, Dr.E.G. Rini (women scientist) and all lab members for providing a friendly and fulfilling environment in the lab along with fruitful discussions. I would especially like to thank Prashant Kumar Mishra (PhD scholar) who has acted as a second guide for me throughout my thesis. This work would not have been accomplished without his support both academically and in the different walks of life.

I'd like to take this chance to express my gratitude to all staff members of IIT Indore for providing all comfort and convenience and all my classmates for their moral support and academic discussions.

***DEDICATED TO MY LORD,  
TEACHERS AND MY FAMILY***

# TABLE OF CONTENTS

Chapter 1.....	13
1.1 Introduction and Background .....	13
1.1.1 Transition metal oxide (NiO) .....	13
1.1.2 Fundamental properties.....	15
1.1.3 Applications .....	19
S1.3 Literature survey: Zinc Titanate ZnTiO <sub>3</sub> (ZTO).....	22
1.4 Objectives and scope of the work.....	23
Chapter 2 .....	25
Experimental Materials and Procedures.....	25
2.1 Sample synthesis: a sol-gel method.....	25
2.1.1 Synthesis of Al/Li codoped NiO: .....	26
2.1.2 Synthesis of Mn doped ZnTiO <sub>3</sub> :.....	27
2.2 Characterization techniques:.....	27
2.2.1 X-ray powder diffraction and structure analysis using Rietveld refinement.....	28
2.2.2 Raman spectroscopy.....	31
2.2.3 Field emission scanning electron microscopy.....	34
2.2.4 Ultraviolet–visible absorption spectroscopy:.....	37
2.2.5 Set up for UV and Visible Light sensing:.....	38
Chapter 3.....	41
3.1.1 Nonstoichiometric Compounds: Classification and Point Defect Formation .....	42
3.2 XRD analysis.....	43
3.3 Microstructural studies.....	46
3.4 Raman Studies: Spin-Phonon coupling .....	47
3.5 UV-Vis spectroscopy.....	48
3.6 Conductance and UV light sensing doped NiO.....	50
3.7 Pressure dependent I-V Characteristics.....	54
3.8 Electroluminescent Analysis.....	55
3.9 Summary of this chapter.....	58
Chapter 4 .....	59

4.1 Synthesis.....	59
4.2 X-ray diffraction analysis.....	59
4.3 Raman Spectroscopy.....	66
4.4 UV Vis spectroscopy analysis.....	68
4.5 Pressure dependent I-V Characteristics.....	70
4.6 Conclusions.....	71
 Chapter 5	
5.1 Conclusions and Scope for Future Work .....	73
 REFERENCES.....	75

## LIST OF TABLES

Table 1: - phase percentage ratio with concentration and atomic position.....	68
---	----

## Table of Figures

Figure 1 ( a) The Ni chains are depicted in a simplified form.	15
Figure 2: Schematic diagram of sol-gel process.	26
Figure 3 A schematic view of Bragg's law is presented ..	28
Figure 4. Quantum energy diagram for Raman scattering.	32
Figure 5 Schematic diagram of Raman spectrometer.	33
Figure 6 Field Emission Scanning Electron Microscope Schematic Diagram.	36
Figure 7 Experimental set-up used for the field-effect scanning electron microscope equipped with the energy dispersive x-ray spectroscopy. #1 Complete arrangement of the FESEM. #2 Connected computer system running user-friendly software. #3 EDX measurement system. #4 It is a complete set of the gold sputtering. #5 Enlarged part of the sample holder of the gold sputtering system.	36
Figure 8 Schematic diagram for UV to Visible light sensing set	39
Figure 9 Point defects	42
Figure 10 X-ray diffraction patterns of $\text{Ni}_{0.9844}(\text{Al}_x\text{Li}_{1-x})_{0.0156}\text{O}$ ( $0 \leq x \leq 1$ ) Inset (a) depicts a systematic XRD pattern; inset (b,c) depicts a plot depicting the change of lattice parameters and bond length substitution with x; and inset (d) depicts the variation of crystalline size and strain with substitution with x.	45
Figure 11 Rietveld refinement fit of $\text{Ni}_{0.9844}(\text{Al}_x\text{Li}_{1-x})_{0.0156}\text{O}$ ( $0 \leq x \leq 1$ ) annealed at 600 °C.	46
Figure 12 SEM micrographs for (a) S0 (b) S1 (c) S2 and (d) S3 samples, serially.	47
Figure 13 The room temperature Raman spectra for $\text{Ni}_{0.9844}(\text{Al}_x\text{Li}_{1-x})_{0.0156}$ samples annealed at 600 °C; Evolution of (b-d) the plot showing the variation FWHM and intensity with x.	48
Figure 14 The UV-Vis absorption spectra for $\text{Ni}_{0.9844}(\text{Al}_x\text{Li}_{1-x})_{0.0156}$ samples annealed at 600 °C.	49
Figure 15 Current changes dynamically for various x	53
Figure 16(a) the variation of fast and slow response and recovery times as a function of substitution x.(b) Displays the evolution of growth and decay currents as a	

function of substitution x.(c) $\Delta I$ variation with substitution.(d) sensitivity with substitution.	53
Figure 17 pressure vs current plots at different constant voltages	54
Figure 18 Electroluminescent spectra	57
Figure 19 Electroluminescent spot	57
Figure 20(a) the XRD pattern of $ZnTi_{1-x}Mn_xO_3$ x=0%, 0.125%, 0.25%, and 0.50% and (b-c) the zoomed view of one peak at $2\theta = 35^\circ$ .	60
Figure 21 Refinement of XRD data via Rietveld for $ZnTi(1-x)Mn(x)O_3$ x=0(a), 0.125(b), 0.25 (c), and 0.50.	61
Figure 22(a) <i>Percentage ratio of phase with substitution</i> (b) the strain and size of $ZnTi(1-x)Mn(x)O_3$ with substitution	63
Figure 23 The lattice parameters variation with substitution.	63
Figure 24 Bond angle variation with substitution.	65
Figure 25 Bond angle variation with substitution.	66
Figure 26 <i>The Raman spectra of <math>ZnTi(1-x)Mn(x)O_3</math> .</i>	67
Figure 27 Raman fitted data of $ZnTi(1-x)Mn(x)O_3$	68
Figure 28 The band-edge from the UV-vis spectra	69
Figure 29 decrease of electronic band gap with substitution.	70
Figure 30 Pressure Vs Current plot at (a) 1 V (b) 2V (c) 5V (d) 10 V	71



## Chapter 1

# Introduction

## 1.1 Introduction and Background: -

From precious stones to fundamental scientific interests, oxides have been a major part in the research field of chemistry, physics, material science, electronics, electrical engineering, etc. Transition metal oxides demonstrate a diverse range of exotic characters which includes high- $T_C$  superconductivity, ferromagnetism, gas sensing, magnetoresistance, magnetocapacitance. Keeping exotic features of simple and complex oxides in mind, we have focused on the study of transition metal and multifunctional oxides. There are approximately more than 100 elements, and every element has a unique electronic configuration, which is determined by its 3-D electron distribution, atomic number ( $Z$ ) and energies. These elements can be categorized as metallic, gaseous, or nonmetallic solids. Therefore, each element is alloyed with other elements and forms new materials. These are classified as metals, semiconductors, ceramics, and polymers. Each class has its distinct properties, i.e., in metals, delocalized electrons provide the force that holds the positive ions together and the bonding is metallic. In semiconductors, strong covalent bonds are formed between atoms (e.g., Si, Ge, GaAs, CdTe, and InP). Polymers consist of different organic atoms and molecules attached with very long C-based chains. Ceramics are solid compounds that are made by sintering. Due to their versatile properties, they really are used in a wide range of uses, e.g., electronic and manufacturing industries [1], [2]. Keeping exotic features of simple and complex oxides in mind, we have focused on the study of transition metal and multifunctional ilmenite oxides.

### 1.1.1 Transition metal oxide (NiO)

When compared to their bulk counterparts, transition metal (TM) oxide nanostructures have gained a lot of scientific interest because of their unique optical, electrical, and magnetic properties. [3,4]. Dilute magnetic semiconductors

such as NiO, TiO<sub>2</sub>, ZnO, Fe<sub>2</sub>O<sub>3</sub>, and CuO find application in pharmacy, electronic, catalyst, solar energy conversion, sensing, and so on [5,12]. Among these, NiO is extremely important due to several reasons, such as comparatively low resistivity [13,14], Nano metal oxides are receiving a lot of attention from researchers because of their wide range of uses. They have a substantially bigger surface area due to their smaller size, making their optical and electrical properties particularly sensitive to surface form. Nickel oxide (NiO) nanoparticles have received a lot of attention among the numerous nanometal oxides due to their exceptional chemical properties and favorable opto-electrical properties. The cubic structure of NiO makes it an antiferromagnetic material. It's band gap of 3.6–3.8 eV [15], which can be altered by reducing the size of the material and/or doping it. As a result, antiferromagnetic materials [16], p-type transparent conducting films [17], electrochromic display materials [18], and chemical segregation materials [19] all use NiO.[19]. Among all transition metal oxides, NiO nanostructures have received huge scientific interest due to their extremely important unique properties. This is the building block of high-*TC* superconductors and giant magnetoresistance compounds. NiO nanoparticles are widely used in optoelectronics, photodetectors, gas/biosensors, field emissions, supercapacitors, photocatalysis, magnetic storage media, and Li-ion batteries. The magnetic properties of NiO can be manipulated by various dopants such as Fe, Mn, or Fe/Li co-substitution to achieve desired functionality and applications. However, there are numerous debates over the origins of room temperature ferromagnetism in this system. Magnetic properties based on the synthesis methods, annealing, Considering the conditions of processing. Therefore, variation in synthesis routes may be responsible for differing reports on the magnetic nature of NiO. Hence, to understand the studies on electronic and magnetic nature of NiO are explored in this thesis.

### **1.1.2 Fundamental properties**

#### **Crystal structure:**

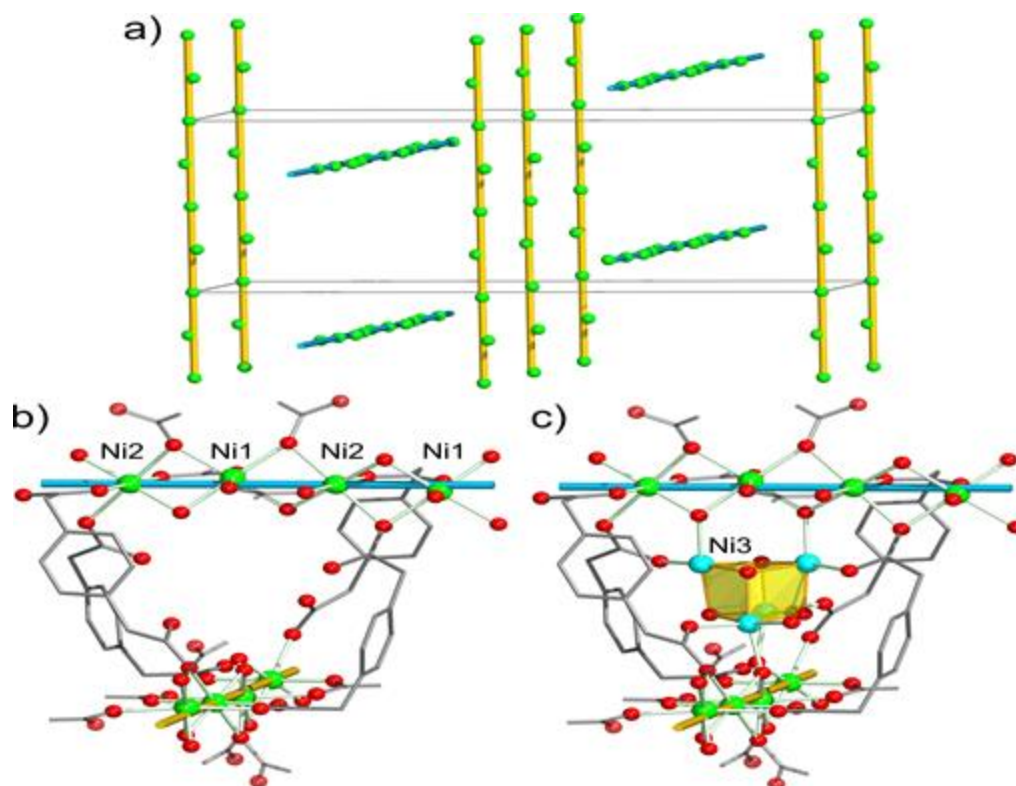


Figure 1 ( a) A simplified diagram of Ni chains in the crystal lattice of 1, with the outlines of one unit cell running along a (light blue rods) and b (orange rods) (gray lines). ( b) A section of 1 that emphasizes the perpendicular Ni chains' connections. ( d)The Ni<sub>4</sub>O<sub>4</sub> cubane unit has been added to the same fragment. Green is Ni<sub>chain</sub>, light blue is Ni<sub>cube</sub>, red spheres are O, and grey sticks are C. [The figure has been taken from *Nadeem et al., Chem. Eur. J.* 2020, 26, 7589 – 7594]

NiO nano powders are black in color and have a cubic structure [Figure 1] with  $Fm-3m$  symmetry. The structure of NiO is like that of NaCl, with octahedral Ni<sup>2+</sup> and O<sup>2-</sup> sites. The rock salt structure is a conceptually straightforward structure. NiO, same as many other binary metal oxides, is frequently non-stoichiometric [20], which means the Ni:O ratio is not always 1:1. This non-stoichiometry in NiO is followed by a color change, with the stoichiometrically correct NiO being green and the non-stoichiometrically correct NiO being red. It is unique 3d transition-metal monoxides, which crystallize in the rock salt structure

with much higher symmetry in contrast to NiO. This reveals that the electronic structure NiO is fundamentally different from CuO or CoO.

It has four formula units per unit cell. Both Ni<sup>2+</sup> and O<sup>2-</sup> ions are octahedrally coordinated [21]. Ni<sup>2+</sup> ions are sixfold coordinated with six O<sup>2-</sup> ions situated at the corners of an octahedral shape. The Ni<sup>2+</sup> and O<sup>2-</sup> ions occupy 4*b* (0,1/2, 0) and 4*e* (0, *y*, 1/4) Wykoff's sites, respectively. The unit cell parameters are  $a = b = c = 4.178 \text{ \AA}$ ,  $\alpha = \beta = \gamma = 90^\circ$  with volume =  $72.92 \text{ \AA}^3$  [22]. The Ni–O, bond distance is  $2.0842 \text{ \AA}$ .

### **Electronic structure:**

Density Function Theory (DFT) suggested that NiO can be both direct and indirect bandgap semiconductor with band gap values of 3.56 eV and 3.5 eV, serially, [23,24]. The distinction between the energy states of the maxima of the valence band (VB) and minima of the conduction band (CB) constitutes the energy bandgap. Both valence and conduction band states are derived from Ni 3*d* orbitals [25,26,27]. Experimentally, the values of the bandgap are observed in the range of 3.5–4 eV [28,29]. Thus, theory matches with an experiment in some cases. Native defects are usually found in semiconductors and play a significant role in electronic properties. The optoelectronic characteristics of stoichiometric NiO, oxygen-rich NiO with Ni vacancies (NiO:V<sub>Ni</sub>), and Ni-rich NiO with O vacancies were compared in a systematic investigation (NiO:V<sub>O</sub>). According to computational studies, both NiO systems with vacancies exhibit gap states. NiO:V<sub>O</sub> gap states are mostly Ni 3*d* states, whereas NiO:V<sub>Ni</sub> gap states are a mix of Ni 3*d* and O 2*p* states. When compared to NiO and NiO:V<sub>O</sub> samples, the NiO:V<sub>Ni</sub> sample's absorption spectra reveal strong defect-induced characteristics below 3.0 eV. The rise in sub-gap absorptions in NiO:V<sub>Ni</sub> is due to gap states in the electronic density of states. The link between native vacancy defects and NiO electrical and optical properties is discussed, indicating that at equivalent vacancy levels.

## **Optical properties:**

Optical properties are key parameters for metal oxides for optoelectronic device NiO nanoparticles emit a prominent green band at 2.37 eV, which covers 80 percent of the integrated intensity of PL spectra. This odd phenomenon is hypothesized to be caused by photogenerated holes trapped in the deep level oxygen vacancy recombining with electrons trapped in a shallow level just below the conducting band . In pure, there have been reports of stoichiometric NiO emissions in the UV band at 346 nm (3.58 eV) [29]. This collection of nanoparticles emitted a wide range of emission bands, ranging from ultraviolet to visible, demonstrating that NiO nanoparticles are highly defective. Deep-level-emission (DLE) green luminescence is a defect-related green luminescence of NiO nanoparticles dominates the PL spectra ~520 nm (~2.38 eV), At 333–357 nm (3.47–3.72 eV), UV emission from the near-band-edge (NBE) is moderate but ubiquitous. UV emission is caused by exciton recombination, which corresponds to NiO's NBE transition [30], whereas DLE in the visible range, classified as DLE1 through DLE3, is caused by structural defects such as interstitial defects and oxygen vacancies.

When microscopic particles with significant nickel vacancies on the surface are excited, the electron hole recombination process is prevented, resulting in lower intensity. Thermal annealing, on the other hand, causes greater electron hole recombination, resulting in higher intensity UV band emission in large particles. Because all the NiO nanoparticles emit red light at normal temperature, they could be used in optoelectronic nanodevices such as light-emitting diodes or laser diodes that emit red light. [31].

For this application, materials should have a high absorption coefficient in the visible range. NiO films are very useful as solar cells with an absorber layer. The band gap of NiO nanostructures is red shifted as compared to the bulk counterpart [27]. Different band gap ranges are reported in the vicinity of 3.5–4.0 eV. For well-aligned arrays of NiO nanoplates, a bandgap of ~3.4 eV was reported

[28]. Thus, NiO has absorbance throughout the visible spectrum extending into the UV region. Using diffuse reflectance spectroscopy, the optical band gap of the NiO nanoparticle was determined to be roughly 4.47 eV, and the photoluminescence emission spectra of our as-synthesized sample displayed a prominent peak at 3.65 eV ascribed to the band edge transition.

Absorption techniques are commonly used to explore the optical characteristics of NiO nanoparticles. Near-band-edge (NBE) and deep-level-emission (DLE) in nickel oxide (NiO) nanoparticles of various sizes are influenced by nickel/oxygen vacancies and interstitial defects. Excitonic recombination at NiO's near-band-edge (NBE) transition induced ultraviolet (UV) emission, while structural defects such oxygen vacancies and interstitial defects induced deep-level-emission (DLE) in the visible range.

### **Vibrational properties:**

Raman spectroscopy examines the phonon vibrations of a lattice. Vibrational properties and spin phonon coupling are studied by this technique and depends on inelastic scattering of a monochromatic light [32]. Under visible and UV illumination, the Raman spectra of NiO is shown. The TO and LO phonon modes are represented by faint peaks in the ranges of 350 cm<sup>-1</sup> to 410 cm<sup>-1</sup> and 520 cm<sup>-1</sup> to 580 cm<sup>-1</sup>, respectively. 2TO (738 cm<sup>-1</sup>), 2LO (1142 cm<sup>-1</sup>), and a combination of TO þ LO (913 cm<sup>-1</sup>) phonon modes are ascribed to the stronger second-order peaks.

### **Electrical properties:**

NiO is an important component of nanoelectronics application. The conductivity of a material is influenced by the structural changes including grain size, grain boundary, and type of the dopant. [33,34]. Hence, the electrical properties of NiO are affected by various synthesis routes, annealing temperature, and growth conditions. Acetate produced NiO films show high conductivity of ~10<sup>-5</sup> S/cm. However, Cu 2-ethyl hexanoate and naphthenate produced NiO films reveal lesser conductivity of 10<sup>-6</sup>–10<sup>-4</sup> and 10<sup>-3</sup>–10<sup>-5</sup> S/cm [35,36]. Electrical conductivity,

mobility, and carrier concentration of NiO increase with increasing temperature [37]. Electrical properties can also be adjusted by altering the stoichiometry and crystallinity of NiO films during the deposition process, which are influenced by  $pH$ , ion pressure, and concentration during film deposition [38].

### **1.1.3 Applications**

NiO is a promising candidate for a variety of purposes including optical and electronic devices. It is abundant in nature, non-toxic, and thermally stable. Its electrochemical properties and low-cost production are extra advantages of its applicability. These combined properties enable NiO nanomaterials to be a potential candidate for several applications such as high- temperature superconductors, emitters, solar cells, gas sensors, magnetic storage media, varistors and catalysis, antimicrobial activity, photoelectrochemical cell, and Li-ion batteries[39].

#### **Solar cells and light-emitting diodes (LED's):**

NiO has been widely used in photovoltaic applications [40]. NiO thin films are potential materials for solar dye-sensitized cells and light-emitting diodes. In the search for a clean and economical energy source, NiO is receiving growing interest from the scientific community. NiO may be used as a solar cell absorber for direct solar energy transformation into electricity. Although the theoretically achievable efficiency for NiO based solar cells is 22.1%, so far, the maximum working efficiency is 2.30%. Hence, a lot of research still needs to be done to achieve better efficiency. NiO is rapid, OLEDs (organic light-emitting diodes) are a type of organic light-emitting diode [41]. To overcome the hole injection barrier, NiO is used as a hole injection layer in various diodes [42]. The stoichiometry of NiO has many defects (VO, VNi). These defects act as an additional energy level within the bandgap NiO which may result in increasing the hole injection efficiency [43]. Also, good quality nanostructures with a high surface area may improve the effectiveness of NiO based solar cells.

### **Photocatalytic activity:**

Water pollution is a major problem in today's world because many organic compounds in wastewater are poisonous and unable to degrade by themselves. Semiconductor catalysts can be effectively utilized under solar UV or visible light to decompose these organic compounds without much complication. NiO is one promising material for degradation of organic contamination and for water splitting because of its narrow bandgap [44]. NiO generates electron-hole pairs under visible light illumination. This process further creates hydroxyl radicals ( $\cdot\text{HO}$ ) from water, which can mineralize organic components [45]. In the water splitting process using NiO, holes which are majority carriers oxidize water to  $\text{O}_2$  and the photogenerated minority electron charge carriers reduce water to  $\text{H}_2$ . Addition of a few percentages of  $\text{H}_2\text{O}_2$  in NiO enhances photocatalytic properties of NiO nanomaterials. The shape and size of NiO greatly influence the photocatalyst properties of NiO. *NiO* nanowires have attracted large attention for photocatalytic degradation of organic dyes [45].

### **Supercapacitors and electrodes for lithium-ion batteries:**

NiO is considered as an excellent electrode for supercapacitor applications because of its environmental friendliness and nice capacitive features. Morphology and size of NiO remarkably influence the electrochemical properties [46,47]. Highly mesoporous structure and surface area lead to high specific capacitance. Li-ion batteries are an important class of batteries and may fulfill the increasing demands of batteries for laptops and cell phones. Materials based on metal oxides, such as  $\text{Fe}_2\text{O}_3$ ,  $\text{Fe}_3\text{O}_4$ ,  $\text{CoO}$ ,  $\text{Co}_3\text{O}_4$ ,  $\text{Mn}_x\text{O}_x$ ,  $\text{Cu}_2\text{O}/\text{CuO}$ ,  $\text{NiO}$ ,  $\text{Cr}_2\text{O}_3$ ,  $\text{RuO}_2$ , and  $\text{MoO}_3/\text{MoO}_3$  have been created, as well as the theoretical capacity the  $\text{mAh g}^{-1}$  of these materials ranges from 500 to 1200  $\text{mAh g}^{-1}$ . Transition metal-based phosphides, nitrides, and sulfides have also been created, with capacities ranging from 500 to 1800  $\text{mAh g}^{-1}$ . However, these materials have problems such as significant potential hysteresis and unstable SEI production, making them less useful Li-ion batteries processing [48].

### **Sensing Applications:**

Due to better surface conductivity, NiO has been utilized to sense various chemicals like CO, HCN, and glucose. Specific surface area is a key player in controlling sensitivity. High surface to volume ratio of nanostructured NiO significantly affects sensing properties. Hence, morphology and size are important factors. Aslani *et al.* reported that cloud- like morphology of NiO when compared to other morphologies, the responsiveness and detection limit of those with a high surface to volume ratio are higher. [49]. The high specific surface area of NiO nanostructures provides better sensitivity for detecting HCN. Variation in sensitivity is explained by changes in chemical reactivity of various crystallographic planes.

### **Magnetic applications:**

Magnetic nanoparticles have wide applicability in magnetic fluids [50], magnetic energy storage and information storage [51]. They are used in enhancing the capacity of magnetic tapes, computer hard discs and in magneto-resistance sensors [52-54]. Magnetic nanoparticles are utilized as contrast agents to increase contrast in MRI [54]. They are also used as site-specific drug delivery agents. Ferrofluid of nanoparticles is used in curing tumors [52-55].

Deviation from the ideal chemical composition for a certain compound, distortion in a perovskite can occur due to various reasons. An example of this complex  $ZnTiO_3$  shows structural transitions with increasing temperature:

Above 820°C, the cubic-to-hexagonal transformation proceeds slowly; around 965° to 1010°C,  $ZnTiO_3$  decomposes into  $Zn_2TiO_4$  and  $TiO_2$  (rutile). A single hexagonal phase can be made by heating for 5 hours at 900°C. Both forms have octahedral  $TiO_6$  groups in their structure [64,65,66].

### **1.2.2 Electro ceramics properties:**

Throughout the 20<sup>th</sup> century, ceramics were used in electronics for the gradual development of electronic devices. Electro ceramics are a special category of advanced ceramic materials that are used in various applications, e.g., optical, high resistivity, chemical stability, dielectric, piezo/ferroelectric, and magnetic. The motive of the present work is to explain various properties of ZTO ceramics such as structure and optoelectronic, which are briefly explained below.

### **1.3 Literature survey: Zinc Titanate ZnTiO<sub>3</sub> (ZTO):**

Zinc titanate metal oxides have gotten a lot of attention because of their potential applications as sorbents for coal gas desulfurization, catalysts in liquid phase organic transformations, dielectric and microwave resonators, gas sensors, hydrocarbon oxidation or CO and NO reduction, semiconductor material, photocatalytic material, and paint pigments. ZTO also has a perovskite structure (i.e., ABO<sub>3</sub>). Where the Zn<sup>2+</sup> situated at 8 corner A-site with coordinate (0 0 0), one Ti<sup>4+</sup> placed at the body center i.e. (½, ½, ½) on B-site and six oxygen atoms are situated at the 6-face center with coordination (0, ½, ½); (½, 0, ½); (½, ½, 0) [69].

The compound appeared to transition to crystalline phase as the calcination temperature increased, and cubic ZnTiO<sub>3</sub> phase was observed at 600C. In the temperature range of 700°C to 900°C, partial phase transition of cubic phase ZnTiO<sub>3</sub> into hexagonal ilmenite type ZnTiO<sub>3</sub> was found. Both cubic and hexagonal ilmenite phases dissolved at 1000°C, yielding cubic Zn<sub>2</sub>TiO<sub>4</sub> and rutile TiO<sub>2</sub> [70].

## **1.4 Objectives and scope of the work:**

Modified NiO and rare-earth-based perovskites were studied for their structural and electrical characteristics. Cation disorders, valence states and their consequences on the electronic properties of ZnTiO<sub>3</sub> have been studied.

**This thesis is aimed to understand the following issues:**

- The role of Al/Li co-doping on the electrical and structural characteristics of Ni<sub>0.9844</sub>(Al<sub>x</sub>Ga<sub>1-x</sub>)<sub>0.0156</sub>O .
- Pure and doped synthesis of ZnTiO<sub>3</sub> samples.
- Structural analysis of ZnTiO<sub>3</sub> and the impact of transition metal ions doping on its structural properties(strain, lattice parameter etc.)
- Optical properties of ZnTiO<sub>3</sub> such as bandgap and defect states were studied and the effect of doping/co-doping on these properties.
- Study of UV and Visible light sensing properties of doped NiO.



## Chapter 2

### Materials and Experimental Methods

Before investigating any property of any material, it is essential to obtain a single phase of the material. The structural and compositional aspects of  $\text{ZnTiO}_3$  and  $\text{Zn}_2\text{TiO}_4$  are very sensitive to the synthesis conditions. Ordering of B site ions is a key player in affecting electronic and structure properties. In addition, the oxygen stoichiometry is influenced by synthesis routes. Hence, preparation of all compounds under investigation is done with extreme care to tailor the B-site ordering. In this section, the synthesis of Al/Li co-doped NiO, and Mn doped  $\text{ZnTiO}_3$  samples are discussed, along with the overview of fundamentals, experimental set-up used for characterizing samples. The working principle and necessary diagrams are provided.

#### 2.1 Sample synthesis: a sol-gel method

Solid ion particles suspended in a colloidal solution (1 nm–1  $\mu\text{m}$ ) in a solvent is called a sol. A gel is the formation of a semi-rigid mass when the solvent starts to evaporate from the sol and the particles/ions left behind; begin to connect with each other in a continuous regular chain.

Sol-gel is a chemical solution process for preparing powders, ceramics, and other materials. The sol-gel approach takes less time to process and yields a satisfactory result. When compared to the hydrothermal process, spray pyrolysis, and solid-state processes, it has higher control over stoichiometry, purity, and homogeneity. These strategies typically need a longer reaction time and more energy.

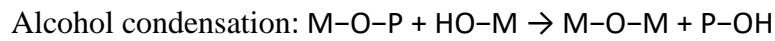
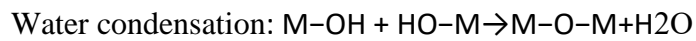
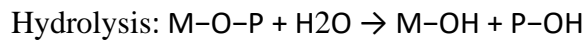
Sol evolves as an inorganic network containing a liquid phase which is known as a gel. Metal oxides are formed by joining the metals with oxo or hydroxy chains. As a result, metal-oxo or metal-hydroxy polymer solutions are formed. The gel is made up of dried to remove the liquid phase from it and finally forms a porous powder. After this, calcination and annealing may be carried out. Generally, water-

soluble for material synthesis, metal nitrates and metal acetates are used as precursors.

The following are the steps in the sol-gel process:

Hydrolysis → Condensation → Gelation → Aging → Drying → Densification

A hydrolysis and polycondensation reaction take place as follows.



A schematic sketch diagram of sol-gel is illustrated in Figure 3. The sol-gel aided combustion method was used to prepare all the samples in this thesis. Samples were thermally treated as per the requirement of phase formation.

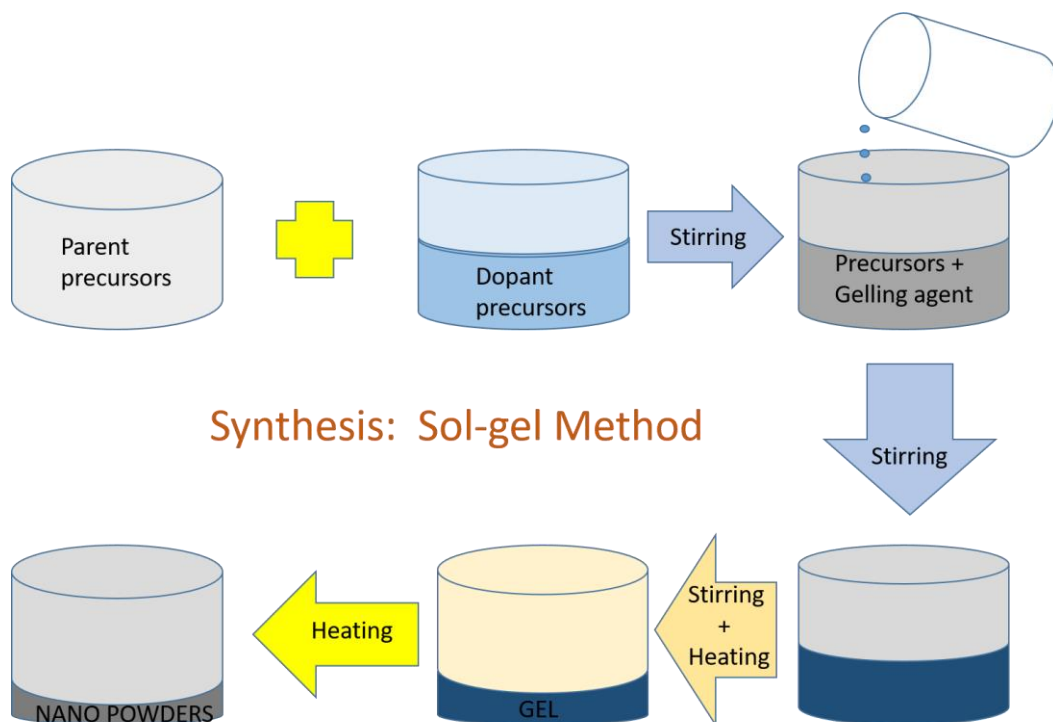


Figure 2: Schematic diagram of sol-gel process.

### 2.1.1 Synthesis of Al/Li co-doped NiO:

To prepare nanocrystalline  $\text{Ni}_{0.9844}(\text{Al}_x\text{Li}_{1-x})_{0.0156}\text{O}$  ( $x=0, 0.25, 0.75$  and 1) powders, Nickel (II) nitrate (99.7%, Alfa Aesar), Lithium(I) nitrate (99.7%, Alfa Aesar) and aluminum (III) nitrate (99.7%, Alfa Aesar), were added according to the stoichiometric ratio. All the precursors were soluble in DI water. A homogeneous solution was prepared by prolonged stirring to function as a gelling agent, a solution of citric acid and glycerol was made in a separate beaker. In a mixed aqueous solution of precursors, the gelling agent was added. The resultant solution was heated to 80 degrees Celsius while stirring to form a gel, which was then dried to provide fluffy black granules. These powders were heated to remove any possible trapped carbonate and nitrate phases.

### **2.1.2 Synthesis of Mn doped ZnTiO<sub>3</sub>:**

For fabricating ZTO, a solution was prepared by dissolving stoichiometric amount of zinc acetate (Alfa Aesar, purity 98.5%) powder was dissolved in DI water, followed by the addition of adequate volumes of titanium (IV) bis (ammonium lactate) hydroxide and manganese nitrate were added according to the stoichiometric ratio. All the precursors were soluble in DI water. Prolonged stirring produced a homogenous solution. 1 gm citric acid (Alfa Aesar, 98%) was used to make a polymeric solution and 1mL of 20% concentrated glycerol (Alfa Aesar, 99.9%) [4]. Thereafter, the obtained solution was heated continuously for 6 to 7 hrs. at a constant temperature of  $\sim 70^\circ\text{C}$ . The burnt gel was finally obtained which was further de-carburized and denitrified at  $500^\circ\text{C}$  for 6h. After this the prepared samples were heated at  $800^\circ\text{C}$  for phase creation, a muffle furnace was used for 6 hours.

### **2.2 Characterization techniques:**

XRD, Raman spectroscopy, UV Vis absorption spectroscopy, and field emission scanning electron microscopy are among the characterization techniques used for structural, local structure, microstructural, and electronic examination (FESEM).

### 2.2.1 Powder x-ray diffraction and structure analysis using Rietveld refinement.

Powder x-ray diffraction is a novel and non-destructive instrument utilized for the structural characterization of crystalline materials that exhibit long-range order. It has numerous applications in scientific, geological, medical, environmental, and industrial fields. In crystallography, powder for x-rays the most common application of diffraction is to determine the kind and number of phases present in a chemical, the unit cell dimensions and crystal structure, crystallite size, texture analysis and residual strain based on their diffraction pattern [71]. The interaction of a monochromatic x-ray beam with the electron clouds of the sample's atoms causes diffraction patterns. Constructive interference only occurs when the difference between travel paths of diffracted rays is equivalent to the number of wavelengths in the radiation as an integral number. This condition is defined by Bragg's law, which relates the angle, and the wavelength incident x-rays and interplanar spacing [72].

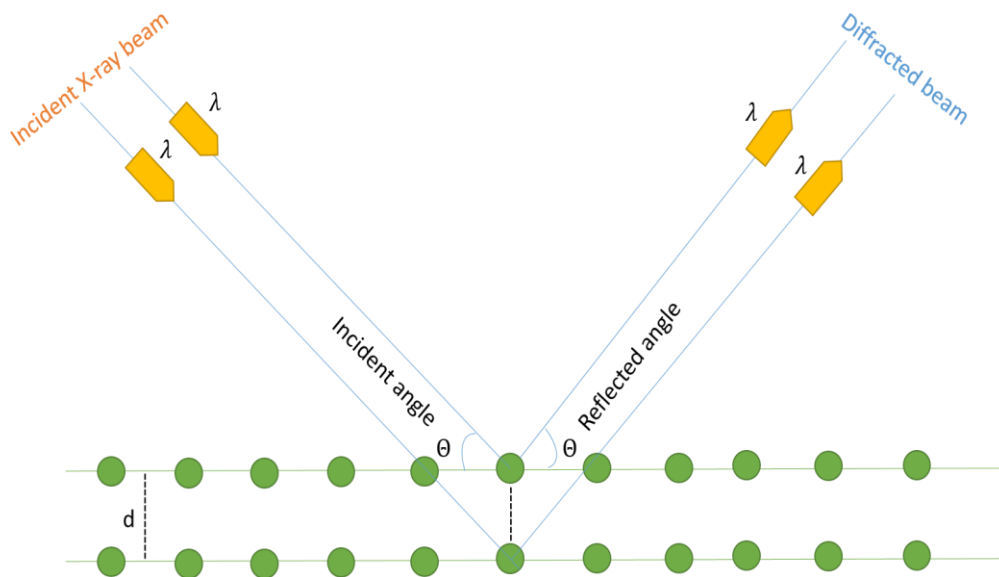


Figure3 :A schematic view of Bragg's law is presented .



instrument parameters may cause the refinement to diverge at early stages. This procedure is only structural refinement and not a structure determination method. The crystal structure, experimental broadening, diffraction optics effects, and other sample parameters (e.g., strain, anisotropy) are all modelled using the proposed model. After refinement, the final crystallographic information files (.cif) can be used as an input file to the Vesta software to get respective bond angles and bond length of constituent elements in the compound. System specifications are as follows:

Model: Bruker D2 Phaser x-ray diffractometer Max Power: 3 kW

X-ray target: Cu anode ( $K\alpha = 1.5406 \text{ \AA}$ ) Operating voltage: 30 kV

Optics: Bragg Brentano, Parallel beam

#### **Analysis using Rietveld refinement:**

Rietveld refinement was performed to quantitatively analyze various physical parameters from the Powder XRD data. Diffraction patterns obtained were compared with the standard CIF files. Rietveld analysis of XRD data was carried for phase analysis using FullProf suite software [75]. It was named after a scientist Hugo Rietveld who developed this method. This is the least-square fit method and takes care of variables influencing the diffraction peaks [76]. The observed diffraction pattern consists of individual reflection planes. Each plane is defined by peak position, peak breadth, and peak intensity which decreases gradually with the distance. The Rietveld approach is a particularly strong method for refining powder diffraction data and, as a result, extracting detailed structural information from the sample. Though the principals involved in the Rietveld profile refinement are rather straightforward, it requires some expertise. The presence of bad starting XRD data points and default instrument parameters may cause the refinement to diverge at early stages. This procedure is only structural refinement and not a structure determination method. The crystal structure, experimental broadening, diffraction optics effects, and other sample parameters (e.g. strain, anisotropy) are all modelled using the suggested model. After refinement, the final crystallographic information

files (CIF) can be used as an input file to the Vesta software to get respective bond angles and bond length of constituent elements in the compound.

### 2.2.2 Raman spectroscopy

Vibrational spectroscopy is the most powerful tool in material science which involves the scattering of electromagnetic radiation by atoms or molecules and can provide qualitative and quantitative structural information for different kinds of compounds with a broad range of physical states. The acquired spectrum provides information about the solid material's structure and behavior. This technique is widely being used to investigate various kinds of modes such as vibrational and rotational in the low and high-frequency region [77]. This technique results in the inelastic Raman scattering when a sample is illuminated with a monochromatic light source using a spectrometer. When a material is bombarded with a high-intensity monochromatic light source, such as a laser, most photons are dispersed off with the same frequency as the incident laser light. Rayleigh scattering is a name for this elastically scattering process. [78]. However, some photons, around 1 photon out of 10 million, have a shift of energy as compared to the original laser energy. In case of a lower or higher energy scattering, this process is called Raman scattering. Raman scattering from atomic vibrations starting from the ground vibrational state produces Stokes's scattering. If the incident photon interacts with a phonon from a vibrationally excited state, an Anti-Stokes scattering takes place which can be visualized by a quantum energy diagram [Figure 5]. The intensity of photons with respect to each energy difference are directly linked to chemical bonds, hence, a spectrum of Raman light can be obtained. Figure 6 depicts a schematic view of a Raman spectrometer.

The following are the basic components of a Raman spectrometer:

**Excitation source (Laser):** a good laser should consist of narrow linewidth and extremely stable output.

**Sample illumination system and light collection optics:** Normally, a laser beam (UV, Visible, or NIR) is shined on the sample, and the scattered rays are collected

with a lens, then transmitted through a spectrophotometer to obtain the appropriate Raman profile of the sample.

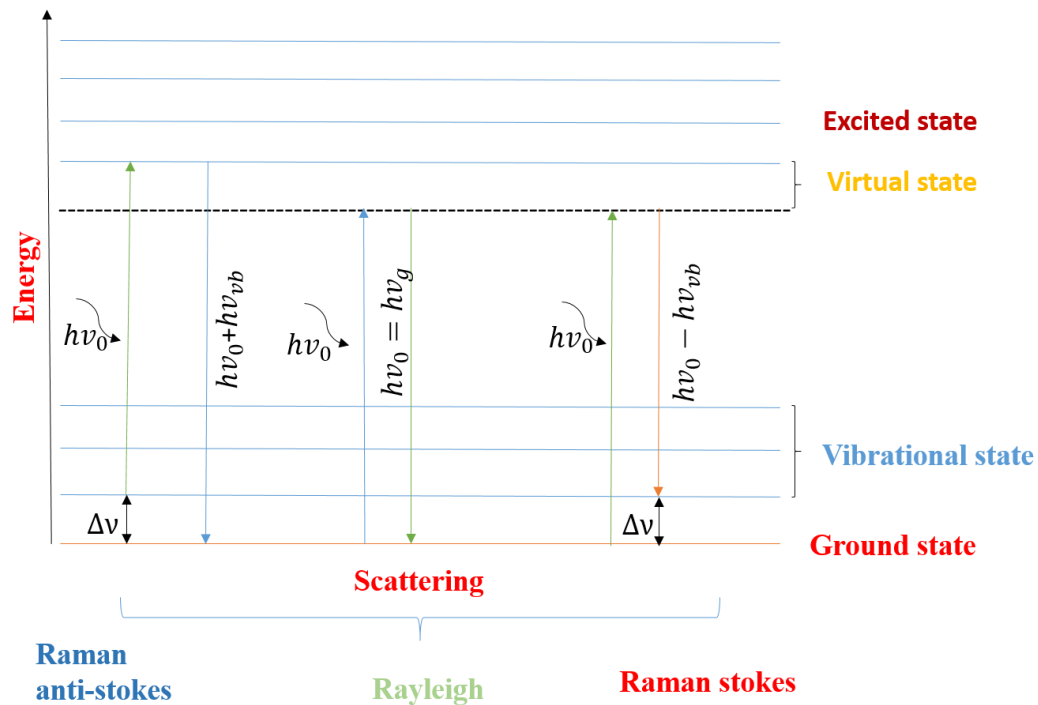


Figure 4. Quantum energy diagram for Raman scattering.

**Wavelength selector (Filter or Spectrophotometer)** is used to separate the incident light spatially according to the wavelength.

**Detector (Photodiode array, CCD or PMT):** Detector is a key component of the Raman spectrometer. A wide selection of detectors is available depending upon the excitation laser being used. A standard CCD is used for visible excitation, a photomultiplier tube (PMT) is utilized for UV excitation, and an indium gallium arsenide (InGaAs) array is well suited for NIR excitation [79, 80]. Raman spectroscopy  $\text{Ni}_{0.9844}(\text{Al}_x\text{Li}_{1-x})_{0.0156}\text{O}$  ( $0 \leq x \leq 1$ ),  $\text{ZnTi}_{1-x}\text{Mn}_x\text{O}_3$  ( $x = 0, 0.125, 0.25, 0.50$ ) a micro-Raman system from Jobin Yvon Horiba LABRAM- HR visible spectrometer was used to analyse the materials. An excitation wavelength of 633 nm was used to measure the room Raman spectra of all samples.

Chapter-2

System specifications:

Make: Jobin Yvon Horibra

Model: LABRAM-HR visible (400–1100 nm) Spectral Range: 50–4000  $\text{cm}^{-1}$

Excitation Laser Sources: He-Ne (632.8 nm) and Argon (488 nm) Detector: CCD detector

Spectral:  $\sim 1 \text{ cm}^{-1}$

Optics: High stability confocal Microscope

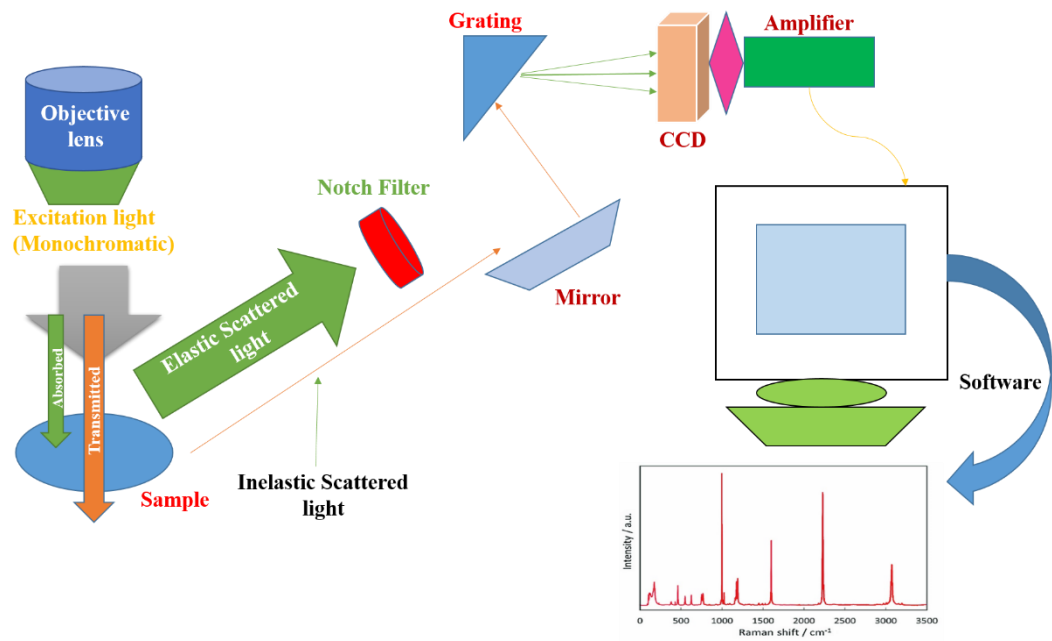


Figure5 Schematic diagram of Raman spectrometer.

### 2.2.3 Field emission scanning electron microscopy

The FE-SEM (Field emission scanning electron microscopy) utilizes a low energy electron beam from a field emission gun to produce the surface image of the sample. This technique is quite useful to measure delicate samples with low melting temperature such as ceramic. Standard scanning electron microscopy is unable to provide reliable information on such samples. An optical microscope is based on diffraction of light, and it has a moderate spatial resolution ~ a few micrometers. To image objects in the scale of nanometers, one needs higher resolution in the range of a few nm, which further requires light of a wavelength in nm. The fine electron beam spot as compared to visible light spot is advantageous to obtain much better spatial resolution. The FESEM provides better and less distorted images with high spatial resolution ~1 nm, which is superior to conventional optical microscopy and SEM.

The collision between the energetic electron and materials results produced Auger electrons, secondary electrons (SEs), backscattered electrons (BSEs), and X-rays etc. FESEM uses SEs and BSEs for construction of images, x-rays for elemental/composition analysis [Figure 8]

**Secondary electrons** (surface morphology): Secondary electrons are used for imaging of the surface of the samples. These originate from near-surface regions (~ 10 nm) of the sample. The mechanism behind the generation of these electrons is by the inelastic collision between the energetically primary electron and the material. Secondary electrons are quite useful for examining the morphology of a sample's surface.

**Back-scattered electrons:** The interaction volume generates back-scattered electrons from a large area. During elastic collisions of electrons and atoms, these Back-scattered electrons are generated. Which leads to a change in the electrons' trajectory. The "billiard-ball" model describes this occurrence, in which small particles (electrons) collide with larger particles (atoms). The number of backscattered electrons that reach the detector is directly proportional to their 'Z'

number, which aids in phase separation. It generates images that transmit information about the composition of the sample.

Energy-dispersive X-ray spectroscopy:

The technique of energy dispersive X-ray spectroscopy (EDS, EDX, and EDXS) was employed to investigate the elemental analyses. It can detect the relative amount of each element and map the distribution of the element. EDX is an integrated part of FESEM. In FESEM the X-ray is generated in a two-step.

**First step:** When an electron beam collides with a sample, it transmits its energy to the sample's atoms. As a result, electrons may be knocked off the atom or jump to a higher energy shell. Holes are formed because of this transition.

**Second step:** Higher energy shell electrons recombine with lower energy shell holes. The energy differential between these two shells was released as x-rays. The generated x- ray is related to the atomic number and a unique property of each element. The energy of these transitions is used to identify the elements.

In the present study, FESEM micrographs were recorded on pellet surfaces of the samples. A Supra55 Carl Zeiss FESEM was used for recording these images. As  $ZnTiO_3$  based materials are highly insulating/nonconductive, therefore a charging effect is prominent. Hence, to avoid the charging effect, a metallic gold deposition ( $\sim 5$  nm) by sputtering techniques was required for charge drainage from the surface. The image of the FESEM setup is shown in Figure 7.

System specifications:

Make: Zeiss Model: Supra 55

Operating voltage: 0.02–30 kV Working distance: up to 100 nA Variable pressure mode: up to 133Pa

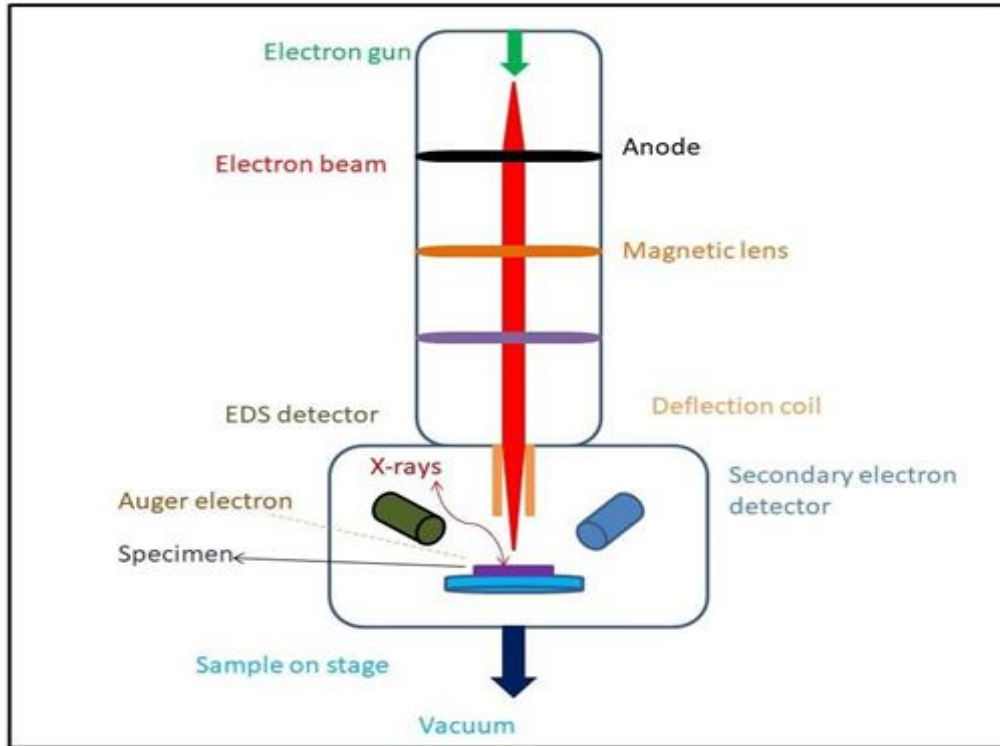


Figure 6 Field Emission Scanning Electron Microscope Schematic Diagram.

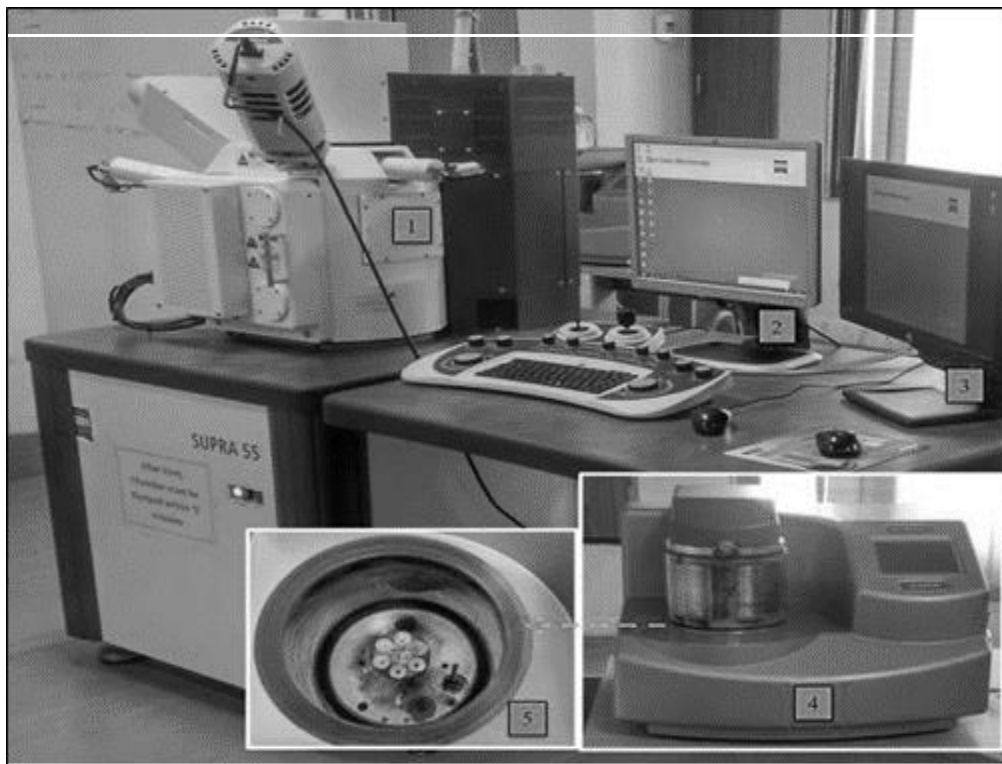


Figure 7 The field-effect scanning electron microscope with energy dispersive x-ray spectroscopy was employed in this experiment. #1 Complete arrangement of

the FESEM. #2 Connected computer systems running user-friendly software. #3 EDX measurement system. #4 It is a complete set of gold sputtering. #5 Enlarged part of the sample holder of the gold sputtering system.

### 2.2.4 Ultraviolet–visible absorption spectroscopy:

In the case of atoms or molecules, electron excitation from lower energy level to higher energy levels is accompanied by the absorption of visible and ultraviolet light. Since all the atoms or molecules have quantized energy levels, only light with the exact amount of energy can cause a transition from one level to another and will be absorbed. As a result, to absorb light in the spectroscopic range 200-800 nm, the molecule should possess an  $\sigma$  bond or atoms with non-bonding orbitals (lone pair of electrons).

When electromagnetic radiation is illuminated on material, various physical phenomena are observed such as reflectance, absorbance, scattering, and fluorescence. Ultraviolet–visible (UV–vis) spectroscopy studies the interaction of UV–vis light with the specimen. This causes an electronic transition of an electron from the filled orbital to the vacant or partially filled orbital when the sample absorbs light of a particular wavelength. This fixed wavelength of light reveals information about the energy bandgap. The absorption of a material at a given wavelength is defined using Beer-Lambert law [79] as:

$$A = -\log \left( \frac{I}{I_0} \right) \dots \dots \dots (2.9)$$

Where I and  $I_0$  are the intensities of the radiation incident and transmitted through the sample. The amount of absorption (A) is proportional to the number of absorbing species(c) present and the distance travelled by the light through the sample (l).

Kubeka-Munk [80] F(R) represented in the equation can be written in terms of absorption  $F(R) \propto \alpha \propto (h\nu - E_g)^{1/n} / h\nu$  (2.10)

$$(F(R) \cdot h\nu)^n = A(h\nu - E_g) \quad (2.11)$$

Using a Research India UV–Vis spectrophotometer, optical absorption in the range 200–800 nm was investigated at room temperature. The Tauc plots were obtained using Kubelka-Munk [81], [82] technique from the reflectivity data:  $\alpha hv = (hv - E_g)^n$ ; where,  $\alpha$  = the absorption coefficient, A = a constant,  $h\nu$  = incident light energy, and  $n$  = constant.  $n=1/2$  for direct bandgap and  $n=2$  for indirect bandgap. The intercepts of the extrapolated linear sections of the equations were used to calculate the band gaps  $(\alpha hv)^{1/n}$  vs  $h\nu$  plots for both cases.

### 2.2.5 Set up for UV and Visible Light sensing:

UV and Visible light sensing setup are an in-house constructed setup to study the response and sensitivity of the prepared samples when exposed to light of different wavelengths.

The setup consists of Instrumentation :-

- i) UV lamp as the source of UV light of wavelength 290nm
- ii) LEDs of Red, Green and Blue color of wavelengths 640nm, 540nm, 450nm respectively
- iii) A dark chamber to house the sample and the light source.
- iv) Arduino Uno
- v) A PC (computer)

A relay linked to an Arduino UNO is used to link the UV lamp and LEDs to the power source. The Arduino may be configured to regulate the light source's ON and OFF states automatically. The sample is kept in a dark box and the light can fall on the sample. Electrodes are available so that the sample can be connected to a multimeter or source meter. Figure 9 depicts a schematic representation of the UV to Visible light sensor system, as well as photos of various light wavelengths.

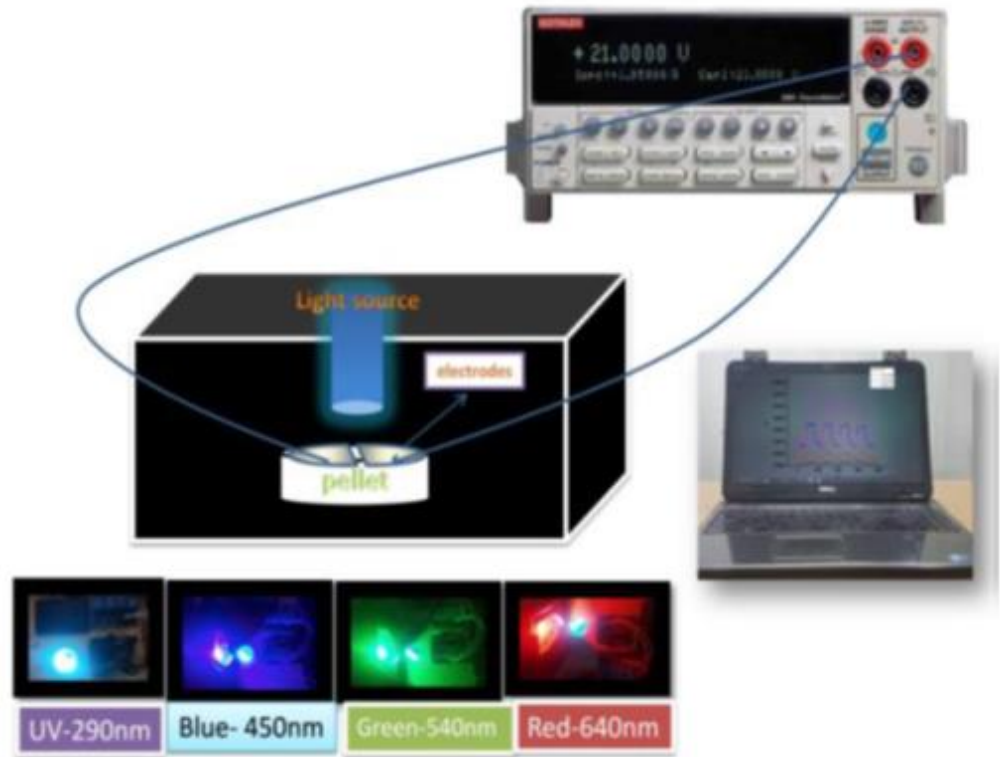


*Figure 8 Schematic diagram for UV to Visible light sensing set*



## Chapter 3

### 3.1 Structural and Electric Studies of Al/Li Substituted NiO

NiO has a cubic rock-salt crystal structure of phase group (Fm-3m). Ni<sup>2+</sup> cations form octahedra with six O atoms. Energy levels of Ni 3d<sup>8</sup> and O 2p<sup>6</sup> are close. Hence, a strong electronic hybridization is possible which enables the material to have a bandgap >3.4 eV. Stoichiometric NiO is insulating. One disadvantage of stoichiometric NiO is the low conductivity that prohibits e-h recombination, therefore reduced hole transport. However, Ni-vacancies can induce intrinsic p-type conductivity. Such compounds are also associated with oxygen vacancies. However, Ni-vacancies have been studied in the presence of both O-rich and O-deficit environments. The formation energy is low for oxygen-rich conditions and high for O-deficit conditions. The conduction mechanism can be conventionally expressed in terms of the band or can be interpreted in terms of small polaron hopping (SPH). In SPH, polarons are formed due to strong interactions between the lattice and carriers. NiO has a very wide bandgap and had gained attention due to its higher mobility and stability of hole transportation but the problem here is weak built-in field strength. This can be modified by the doping of Lithium because its doping increases the hole extraction level due to its deep valence band edge (-5.3 eV to -5.4eV ) and increases the open-circuit voltage. Lithium doping leads to rapid electron generation leading to the radiative recombination of the electron and holes. This will lead towards electroluminescence. NiO has the possibility to become the phosphor material in the near UV region. It is seen that the EL performance of alternating current devices is a strong function of the crystallinity of the phosphor interface properties, space charge in phosphor, the nature of the luminescent centers, and their coordinates in the host crystal lattice. Solid-state light-emitting devices have been drawn considerable research attention due to their low-power requirements compared with conventional devices. However, to the best of our knowledge, the

effect of Li incorporation on the bandgap of NiO has not been systematically studied well for sol-gel produced Aluminum doped NiO. In the present work, the structural, morphological, electrical, and optical properties of Li doped NiO processed by sol-gel. The results indicate a strong correlation between the conductivity, bandgap modulation, and the plasmonic phenomenon in the NiO. The feasibility of employing nanoparticle NiO is due to its easy synthesis: the synthetic strategy plays a crucial role in modifying the NiO structure, Furthermore, a synergistic effect of the cubic NiO with the Lithium incorporation can amplify the former's performances, prepared by the sol-gel method, exhibiting the enhanced plasmonic. This had altered the defects and has greatly reduced the bandgap with the rapid tuning of the interstitial and the vacancy defects. The Li, in combination with the NiO semiconductor, forms deep level transportation of electrons and helping in scavenging the holes for quick transformation and recombination. Moreover, Li doping results in shifting of the conduction band towards the positive direction narrowing the bandgap. Despite such benefits, there are few reports investigating the impact of the Li dopant and plasmonic phenomenon with the enhanced bandgap tuning and its relationship with the defects.

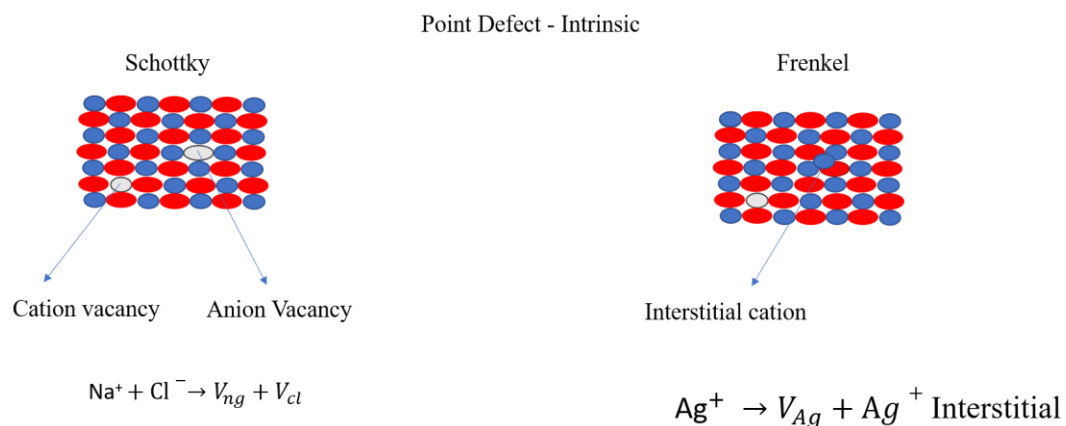


*Figure 9 Point defects*

### 3.1.1 Nonstoichiometric Compounds: Classification and Point Defect Formation

Chemically modified substances have a homogenous physical phase in which unit cell properties vary continuously with content. The free energy of such compounds is determined by the composition and temperature of the system. The chemical potential of a solid is determined by its composition, while structural and thermodynamic properties are influenced by microscopic and macroscopic characteristics. Due to chemical modifications, several properties of the crystallographic cell may alter and can be determined by XRD [84]. Transition metal oxides can be modified by incorporating nitrides and sulfides [85–87]. The compositions of nonstoichiometric compounds are like those of stoichiometric compounds, and they can be represented using formulas like  $\text{WO}_{3-x}$ ,  $\text{Co}_{1-x}\text{O}$ ,  $\text{Zn}_{1+x}\text{O}$ , and  $\text{Ni}_{1-x}\text{O}$ , where  $0 < x < 1$ . In the first situation, an oxygen vacancy would form, and a compensatory metallic vacancy would be associated, as lattice defect states. These lattice defects result in a divergence from an ideal stoichiometric composition. As a result, some nonstoichiometric compounds have anionic vacancies, whereas others include cationic vacancies. These vacancies appear as absence of ions from the regular sites these would have normally occupied.

This chapter's approach is to find promising material for the spintronic sector. Even at room temperature, Al/Li substitution may improve electric characteristics, making such materials appealing for device applications. A single-phase  $\text{Ni}_{0.9844}(\text{Al}_x\text{Li}_{1-x})_{0.0156}\text{O}$  ( $0 \leq x \leq 1$ ) series was synthesized. The samples were named S0 for  $x=1$ , S1 for  $x=0.75$ , S2 for  $x=0.25$  and S3 for  $x=0$ . The structural, electronic, and magnetic properties are explored and analyzed.

### 3.2 X-Ray Diffraction analysis

All the NAL samples were annealed at  $600^\circ\text{C}$ . Rietveld refinement of the X-ray Diffraction (XRD) patterns [Figure 10a] confirms a cubic *NiO* structure of

phase group (Fm-3m) for all the NAL samples. No extra phases other than the *NiO* are observed related to any complex mixed oxides of *Li* and *Al* [Figure 10]. Rietveld analysis was performed using Full-Prof suite software. Acceptable goodness of fit ( $\chi^2$ ) values was obtained for all the samples. The analysis confirms the *NiO* (Fm-3m) phase [Figure10a]. Lattice parameters ( $a=b=c$ ) initially increased from  $\sim 4.175\text{\AA}$  in *S0*, to  $4.184\text{\AA}$  in *S3*, reduced to  $4.168\text{\AA}$  in *S4*. A significant change in the lattice constants were observed for all samples [Figure 10b]. The octahedrally bonded *Ni* and *O* atoms form *NiO6* octahedra. The ionic radii of the host  $Ni^{2+}$  ( $0.83\text{\AA}$ ) is larger than  $Al^{3+}$  ( $0.675\text{\AA}$ ) but smaller than  $Li^{1+}$  ( $0.90\text{\AA}$ ) in the VI coordination state. Because of the higher cationic charge of  $Al^{3+}$  than the host  $Ni^{2+}$ , extra oxygen may be introduced into samples *S0*, *S1*, *S2*, and *S3* to maintain charge balance in the lattice. This could result in oxygen interstitials, which could cause lattice expansion. However, in the solely  $Li^+$  doped sample, *S4* due to its lesser charge (+1) than  $Ni^{2+}$ , the amount of oxygen vacancy can be increased. Hence, the sudden lattice contraction can be correlated to removal of oxygen from the lattice.

Bond lengths and angles are influenced by this interplay of oxygen vacancies and interstitials in the series due to the varying proportions of  $Al^{3+}$  and  $Li^+$  [88]. The expanding and contracting bond length parameters are connected to lattice strain. The bond length increases for samples *S0*, *S1*, *S2* and decreases for sample *S3* [figure 10(c)]. The similar trend of variation was observed in lattice constants and bond lengths as predicted. Strain is correlated with lattice disorder and therefore to long range order. It has been found that a less strained lattice has bigger crystallite sizes and shorter bond lengths, and vice versa [89]. Tinny tool software was used to estimate strain and crystallite size, followed by the Williamson Hall-method and the Scherer equation. The crystallite size was observed to decrease for samples *S0*, *S1*, *S2* and increase for sample *S3* while the lattice strain increases for sample *S0*, *S1*, *S2* and decreases for sample *S3* [figure 11(d)]. The host  $Ni^{2+}$ (VI) [ $0.83\text{\AA}$ ] is larger than  $Al^{3+}$ (VI) ion [ $\sim 0.675\text{\AA}$ ] but smaller than  $Li^+$ (VI) [ $\sim 0.9\text{\AA}$ ]. For *S1* a smaller but higher charged  $Al^{3+}$  ion is incorporated in the lattice. This will invite more oxygen in the lattice thereby at first neutralizing

the latent  $V_O$  and thereby introducing  $O_i$ . This will create a positive pressure on the lattice, thereby increasing the bond lengths and thereby the lattice parameters. This is what was observed from the Rietveld refinement. For  $S_2$  the trend continues due to the presence of  $Al^{3+}$  ion, but the presence of  $Li^+$  ion somewhat compensates for the extra charge. At the same time, the  $Li^+$  ion is larger than the  $Ni^{2+}$  ion which continues to exert the positive pressure on the lattice. However, the effect is somewhat reduced by the loss of oxygen due to the lesser charge of the  $Li$  ion. In the  $S_3$  sample, with increase of a larger  $Li^+$  concentration on one hand there should be expansion of lattice but on the other hand due to its lesser charge than parent  $Ni^{2+}$ , there will be  $V_O$  created in the lattice, which will force the lattice to contract. The lattice strain increased and reduced accordingly and was logical to the analysis of charge and size of the dopants. The crystallite size reduced and increased with the increase and decrease of the lattice strain in these samples.

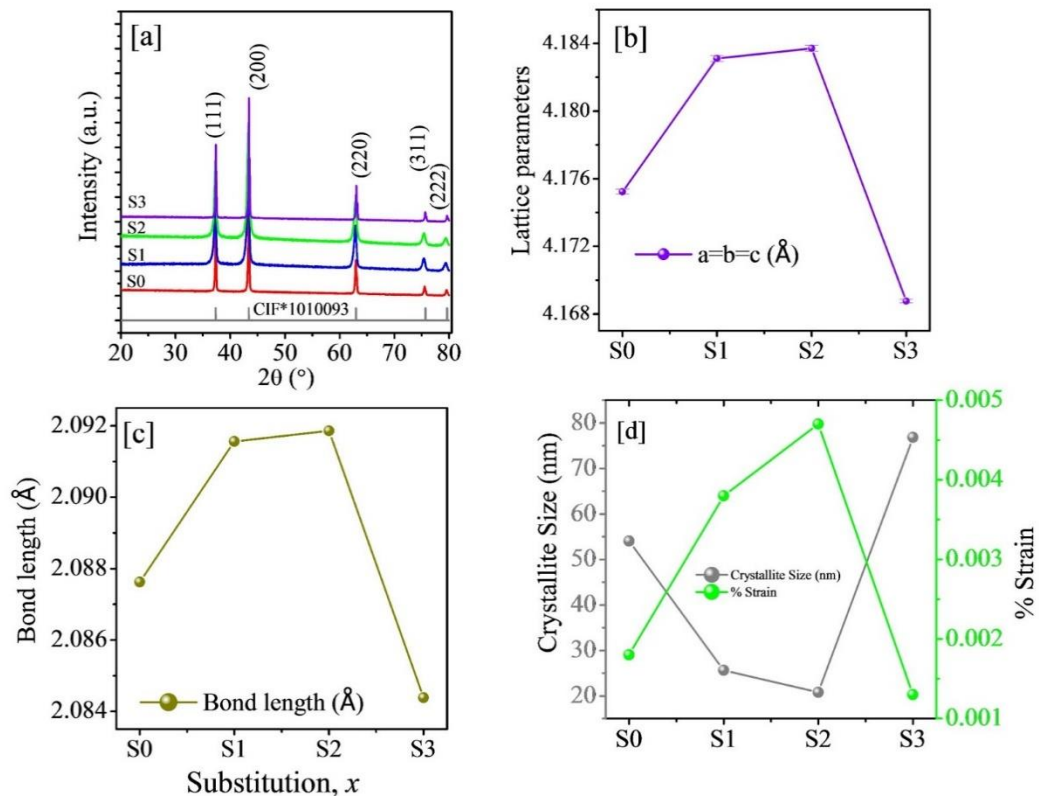


Figure 10 Patterns of X-ray diffraction of  $Ni_{0.9844}(Al_xLi_{1-x})_{0.0156}O$  ( $0 \leq x \leq 1$ ) samples: Inset (a) depicts a systematic XRD pattern; Inset (b) depicts a plot

depicting the variation of lattice parameters  $a=b=c$  with  $x$ ; (c) depicts the variation of bond length substitution with  $x$ ; and (d) depicts the variation of crystalline size and strain with substitution with  $x$ .

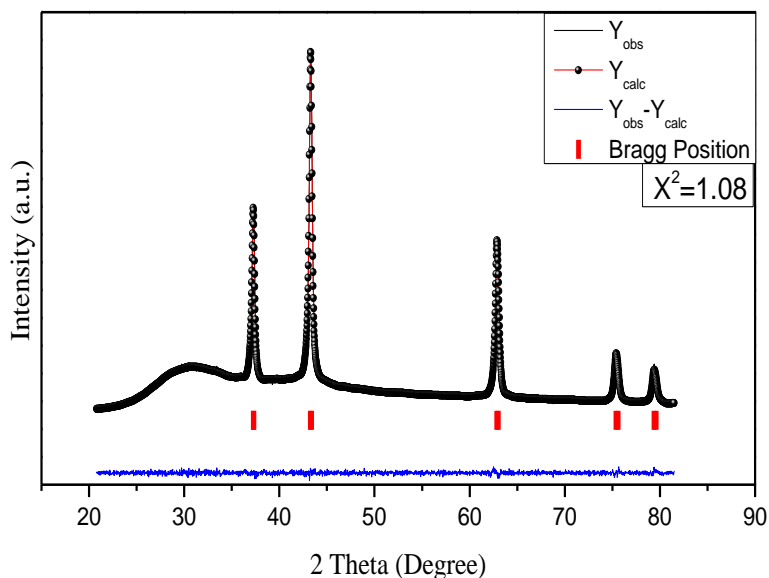


Figure 11 Rietveld refinement fit of  $\text{Ni}_{0.9844}(\text{Al}_x\text{Li}_{1-x})_{0.0156}\text{O}$  ( $0 \leq x \leq 1$ ) annealed at  $600^\circ\text{C}$ .

### 3.3 Microstructural studies

The SEM images for  $\text{Ni}_{0.9844}(\text{Al}_x\text{Li}_{1-x})_{0.0156}\text{O}$  ( $0 \leq x \leq 1$ ) samples are shown in Figure 13. The micrographs show a uniform distribution of grains all through the samples. The FESEM study was performed to investigate the particle size and morphology of all samples. For sample S0 agglomerated spherical particles of  $\sim 20$ - $30\text{nm}$  was observed. However, high quality FESEM images of samples S1, S2 and S3 were observed. ImageJ software was used to calculate the actual particle sizes of S1, S2 and S3. The calculated nanoparticle varies in the vicinity of the  $30$ - $33\text{nm}$  range.

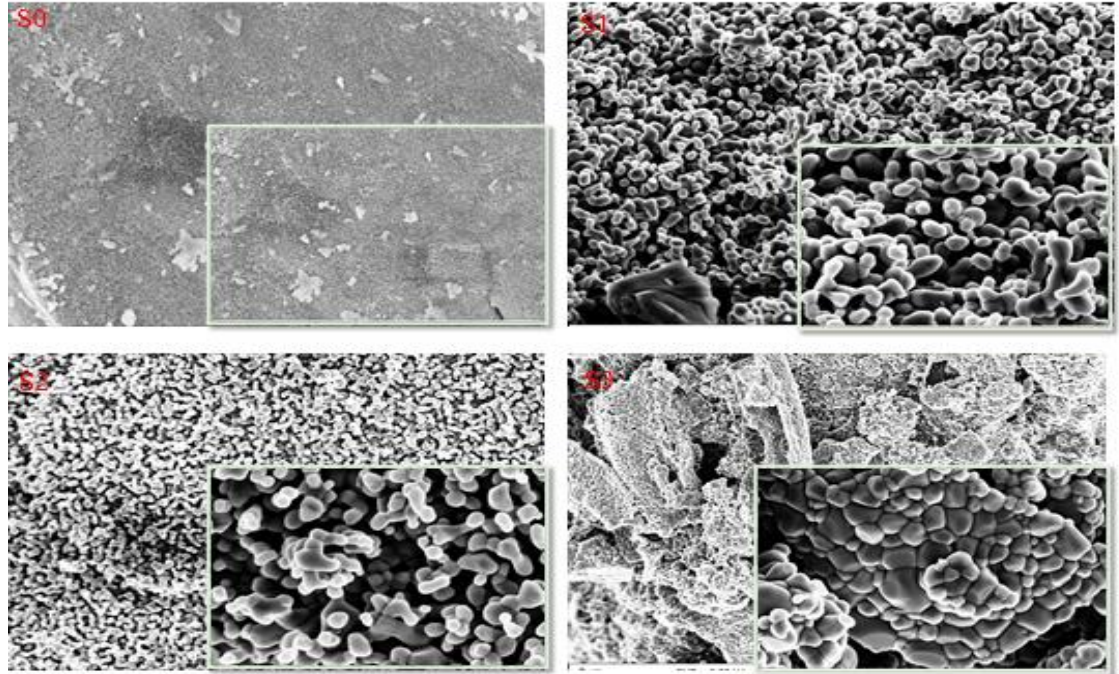


Figure 12 SEM micrographs for (a) S0 (b) S1 (c) S2 and (d) S3 samples, serially.

### 3.4 Raman Studies: Spin-Phonon coupling

Raman spectroscopy is a very useful technique for investigating the lattice vibrations and structural information on the scale of a few lattice constants. Figure [13] shows the Raman spectra of the NAL samples. The band at  $560\text{ cm}^{-1}$  arises from the O–O planar vibrations known as longitudinal optical one phonon-mode (LO). The band at  $1079\text{ cm}^{-1}$  arises from the Ni–O stretching vibrations known as two-phonon scattering (2LO). The high intensity of the 2LO interaction band indicates that NiO has good crystallinity. The increase of FWHM parameters of 2LO mode at  $1190\text{ cm}^{-1}$  indicate the increase of surface defects and hence decrease of crystallite size and increase of lattice strain. The FWHM increase for sample S1, S2 and decrease for S3 hints the decrease of lattice strain and hence defects. It is observed that with introduction of *Li* and *Al* due to higher cationic charge-imbalance, the defects first increase and then decrease for S3. A similar trend of variation of lattice constants and lattice strain was observed in XRD results. It means with introduction of *Li* ion in sample the lattice contracted and hence the defects like  $O_i$  reduced.

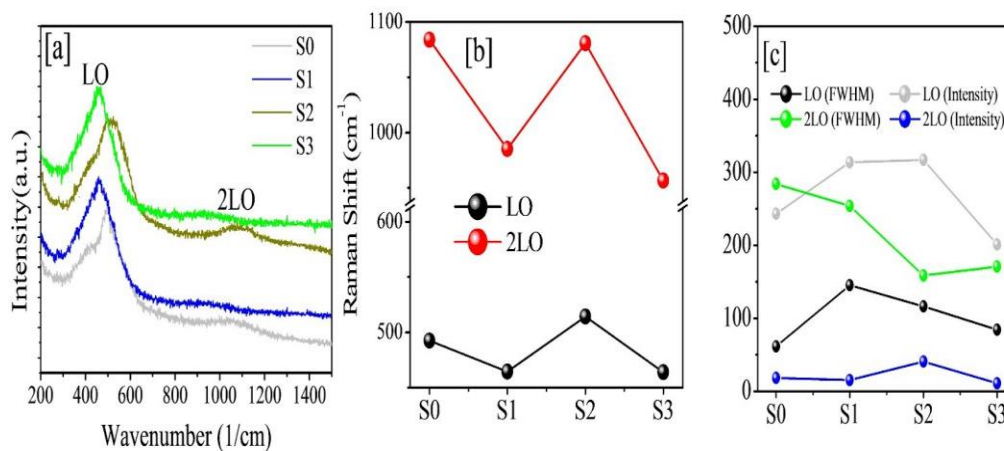


Figure 13 The room temperature Raman spectra for  $\text{Ni}_{0.9844}(\text{Al}_x\text{Li}_{1-x})_{0.0156}$  samples annealed at 600 °C; Evolution of (b-c) the plot showing the variation FWHM and intensity with  $x$ .

### 3.5 UV-Vis spectroscopy Analysis:

To evaluate the band gap and the lattice disorder the UV-vis absorption spectroscopy of the NAL nanoparticles was performed in the 200-1000 nm wavelength range. The diffuse reflectance spectroscopy (DRS) of all the prepared samples was studied in the UV-visible region (200-1100nm) [Figure 14]. The absorption constant,  $\alpha$ , was derived from the percentage reflectance ( $\%R$ ). The Kubelka-Munk function [90 Choudhury, B, Borah, B, Choudhury, A: Ce-Nd co-doping effect on the structural and optical properties of  $\text{TiO}_2$  nanoparticles. Mater. Sci. Eng B 178, 239–247 (2013)],  $F(R)$  was considered as the equivalent to  $\alpha$ , where  $F(R) = (1-R)^2/2R$ , and  $R = \%R/100$  [91]. Interestingly, based on sample absorption spectra S2 and S3 the narrow dip in UV region and broader dip in visible region was observed. However, the absorption dip became broader for both UV and visible regions for samples S0 and S1. As a result, the literature of various materials was reviewed in depth to better understand the diversity in absorption spectra of the samples. The phenomena of Localized Surface Plasmon Resonance (LSPR) are responsible for narrow dip in UV range (300 nm) and broader dip in visible region (400-500 nm) [92]. Dark-field microscopy [93] and Surface

Enhanced Raman Scattering (SERS) [94] are some of the techniques commonly employed to characterize surface plasmons. The absorption spectra were studied in detail. Coulombic interaction between electrons and nuclei produces a restoring force when the electron cloud is shifted relative to its original position. The electron cloud oscillates because of this force. The Localised Surface Plasmons (LSP) has two key effects: it dramatically increases the electric field at the particle's surface, and it maximizes the particle's optical absorption at the plasmon resonant frequency. For samples *S2* and *S3*, the plasmon resonant frequency is maximum from far UV to visible region. However, for samples *S0* and *S1* the plasmon resonance behavior was not observed and hence absorbance in the visible region was absent. It means the charge imbalance in the lattice due to certain proportions of the  $Al:Li$  ion promotes *LSPR* while in certain others it does not. The absence or very less amount of Li ion does not support *LSPR* while for the higher doped and entirely Li-ion doped sample *LSPR* is strong as observed for *S2* and *S3*. Hence, Li has a definite role in promoting *LSPR*. The extra proportion of  $Li^+$  in place of  $Al^{3+}$  will play a strong role creating a disproportionate balance of  $O_i$  and  $V_o$  which may be responsible for such exciting optical properties. This needs a more detailed analysis, with other proportions of the dopants and with other doping level solid solutions. Hence, the presence of  $Li^+$ ,  $V_o$  or  $O_i$  may have a very important role in generating modifications of the electron cloud which may interact with the incident UV visible light and create plasmon resonance in the visible region.

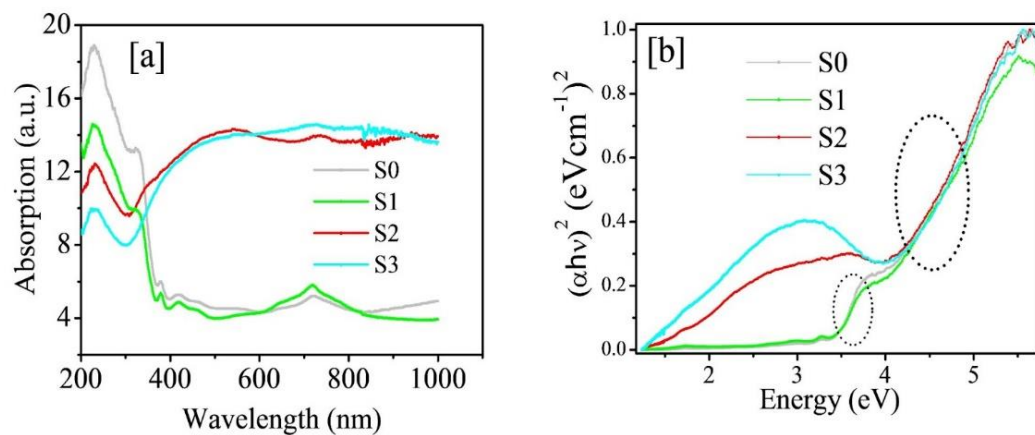


Figure 14 The absorption spectra of UV-Vis for  $Ni_{0.9844}(Al_xLi_{1-x})_{0.0156}$  samples annealed at 600 °C.

### 3.6 Conductance and UV light sensing:

The conductance and current variation dependent on voltage were tested for all samples. From the absorbance nature of samples *S1* and *S3* it is very important to visualize the conductance and dark current of samples. Current-voltage (I-V) properties of samples were tested in applied voltage range of -1 to 1V. The limited range was chosen due to the high conductivity of the doped samples. For higher voltages, a very high current was observed giving rise to luminescence and will be discussed in the next section. With the increase of Li content, the current increased nonlinearly and drastically from *S0* to *S3*.

The higher conductance in Li-added samples, makes them important candidates for UV-sensing properties which were studied using a home-made setup. A UV light source of wavelength ~290 nm and power 11W was applied on the samples in the presence and absence of light. This cycle of illumination was designed for 4 min with the UV light “ON” followed by an immediate 4 min with the light “OFF”. Many cycles were studied to verify the repeatability of the phenomenon and four complete cycles are being reported on which the time-dependent rise and fall of current was studied. The time-dependence of current was analysed using a single exponential fitting of current cycles.

The current increases during illumination following the equation:  $I = I_{max} - I_g \cdot \exp(-\tau/\tau_g)$ ; where,  $I_g$  and  $\tau_g$  are the response or growth current component and time-constant of the samples.  $I_{max}$  is the maximum current in the presence of light. Similarly, the current decayed in absence of light following the equation:  $I = I_{min} + I_d \cdot \exp(-\tau/\tau_d)$ ; where,  $I_d$  and  $\tau_d$  are the decay current component and time-constant of the samples.  $I_{min}$  is the dark current in the absence of light.

The growth time constant,  $\tau_g$ , decreased with Li-incorporation from 187 sec in *S0* to 162 sec in *S1* and 160 sec in *S2* but thereafter increased to 272 sec in *S3*. Hence, with  $Li^+$  incorporation the sensing process becomes faster but with the removal of  $Al^{3+}$  the system becomes much slower. Hence it seems a co-doping of  $Al^{3+}$  and  $Li^+$  helps in making the system respond faster to the UV-

light. Similarly, the decay time constant,  $\tau_d$ , decreased with *Li*-incorporation from 230 sec in *S0* to 186 sec in *S1* but thereafter increased to 270 sec in *S2* and 280 sec in *S3*. Hence, the process revives fastest for the *S1* sample but delays recovery for higher *Li*-incorporated samples.

The dark current, i.e. the minimum current,  $I_{min}$  increased with *Li*-incorporation from 5.20  $\mu\text{A}$  in *S0* to 2.78 mA in *S1*, 9.56 mA and 50.48 mA in *S3*. Hence, with  $\text{Li}^+$  incorporation the sensing current becomes stronger suggesting an increase in the carrier concentration and mobility of the carriers involved in the dark unexcited conditions. On the other hand, the maximum current  $I_{max}$  increased with *Li*-incorporation from 5.73  $\mu\text{A}$  in *S0* to 3.07 mA in *S1*, 10.09 mA and 54.96 mA in *S3*. The difference between the  $I_{max}$  and  $I_{min}$ , given by  $\Delta I = I_{max} - I_{min}$ , represents the sensing photocurrent. The photocurrent,  $\Delta I$ , increases with substitution. However, the increments in the photocurrent and the dark current are not uniformly proportionate, thereby providing an irregular rise and fall of sensitivity ( $\%S$ ), given by  $\%S = \Delta I / I_{min}$  [Figure 16d]. The growth current,  $I_g$ , increased with *Li*-incorporation from 2.55  $\mu\text{A}$  in *S0* to 1.66 mA in *S1*, 2.98 mA and 18.2 mA in *S3*. Similarly, the decay current,  $I_d$ , increased with *Li*-incorporation from 6.17  $\mu\text{A}$  in *S0* to 5.04 mA in *S1*, 5.02 mA and 40.67 mA in *S3*. The increasing trend of the response currents for both growth and decay hint at a mechanism of the charge carriers being affected by the UV-light. Hence, understanding of the mechanism of these current components is essential.

The incorporation of  $\text{Li}^+$  balances the extra *O*-content in the lattice. The larger size of the *Li* ion exerts pressure in the locality of the *Li* ion thereby increasing strain in *S1* and *S2*. However, in these two samples  $\text{Al}^{3+}$  is still present which annihilates the  $V_O$  and generates  $O_i$  defects. Hence, the larger size of  $\text{Li}^+$  creates a positive pressure on the lattice which is the source of the strain. On the other hand, in *S3* the absence of  $\text{Al}^{3+}$  allows the  $\text{Li}^+$  to create ample  $V_O$  so that the lattice becomes devoid of *O* and the pressure due to the larger size of the  $\text{Li}^+$  ion is compensated. Hence, the strain decreases drastically. Most likely the positive lattice pressure is responsible for the faster response to the UV light in

these NAL samples which enables an oxygen adsorption-desorption process at the surface of the nanocrystals to be more efficient.

Metal-oxide-based photo-detectors involve generation/recombination of photo-carriers, and absorption-desorption mechanism. *NiO* is a p-type material with a hole-rich surface due to a chemi-adsorbed oxygen molecule in the air ambient. Electron-hole ( $e-h$ ) pairs are produced due to excitation of incident photons during illumination [ $h\nu \rightarrow e^- + h^+$ ]. By reaching the surface the electrons get in touch with the atmospheric oxygen molecule and starts an oxygen-adsorption process [ $O_2(g) + e^- \rightarrow O_2^-(ad)$ ]. Holes gather in the valence band ( $VB$ ). Adsorption saturates with time as the hole accumulation depth increases thereby saturating the photocurrent. In the absence of illumination, the accumulated holes combine with the adsorbed  $O_2^-$  and thereby releases an  $O_2$ -molecule and an electron. Hence, technically a  $e-h$  recombination takes place. This process is called desorption: [ $O_2^-(ad) + h^+ \rightarrow O_2(g)$ ]. A decay in the photocurrent occurs due to reduction of the hole accumulation layer.

The increase of the  $I_{min}$  and  $I_{max}$  is a consequence of  $Li^+$  incorporation and may be due to a reducing amount of  $O_i$  and subsequent increase of  $V_O$  in the immediate vicinity of the  $Li^+$  ion. However, the increase in  $I_g$  and  $I_d$  in Li-doped samples should be related to increase in the number of UV-excited  $e-h$  pairs in these samples. Such a distinguished phenomenon can be assigned to the increase in  $Li^+$  ions and decrease in  $Al^{3+}$  ions only, as the changes in other defects like  $O_i$  or  $V_O$  are more complex consequences of the substitution process and may not be a straightforward aspect to comment on. Hence, the Li-containing NAL materials with a considerable amount of dark current has the potential to be a highly effective UV-light sensor.

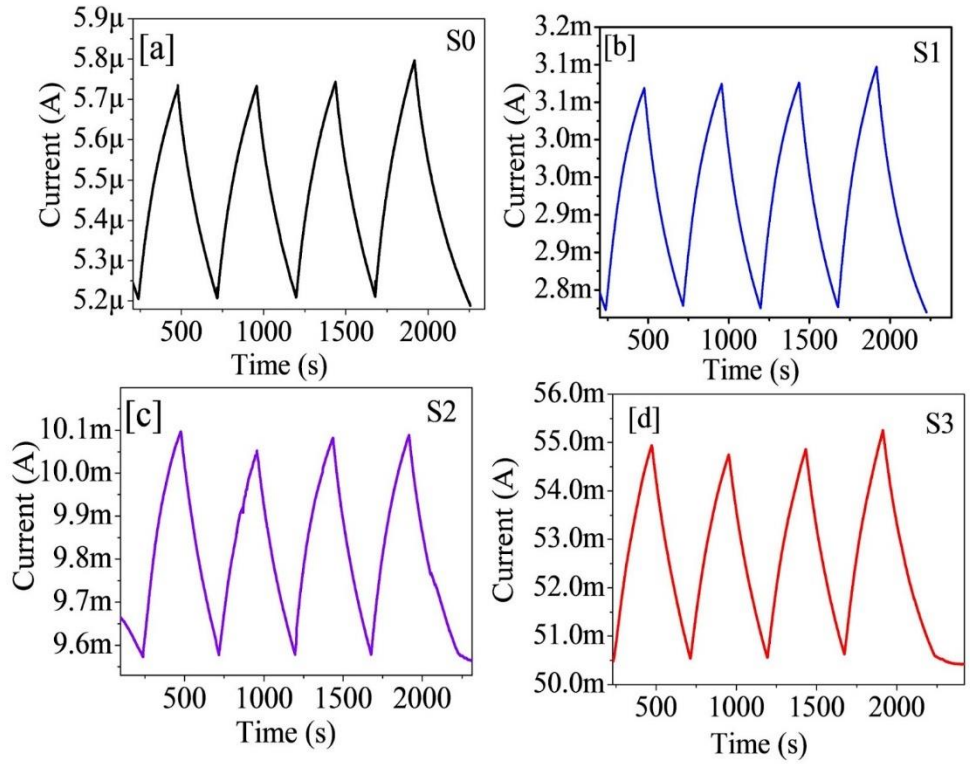


Figure 15 Dynamic changes in current for different  $x$

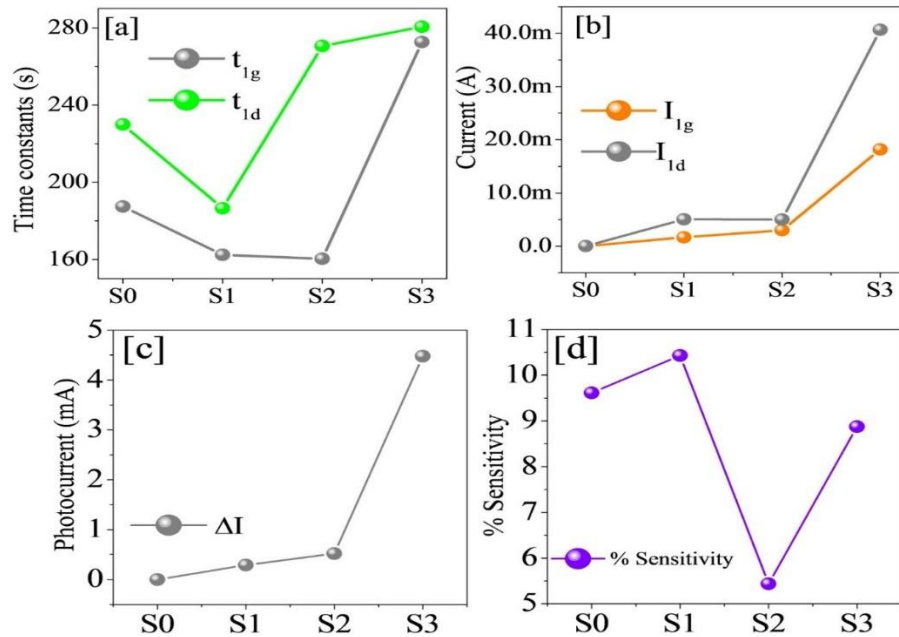


Figure 16(a) the variation of fast and slow response and recovery times as a function of substitution  $x$ . (b) Displays the evolution of growth and decay currents as a function of substitution  $x$ . (c)  $\Delta I$  variation with substitution. (d) sensitivity with substitution.

### 3.7 Pressure dependent I-V Characteristics:

The pressure dependent (1-3 ton/mm<sup>2</sup>) I-V characteristics of all the prepared samples were investigated. The pressure vs current plots at a constant voltage of 0.10V shows that the current increased with increasing pressure [Fig. 14]. Note these results were repeatable and the experiment was performed in several iterations on the same sample followed by similar runs on other specimens of the same composition. This is true for all the samples. The changes are minimal for the *S0* sample. With Al incorporation in *S1*, the current increased. The current increased further for *S2* and for lower pressure values. For higher pressure however, the *S2* sample became more conducting than the *S3* sample. This may be due to the contributions of the electron clouds of the doped elements which lead to several other defects including oxygen vacancies and interstitials.

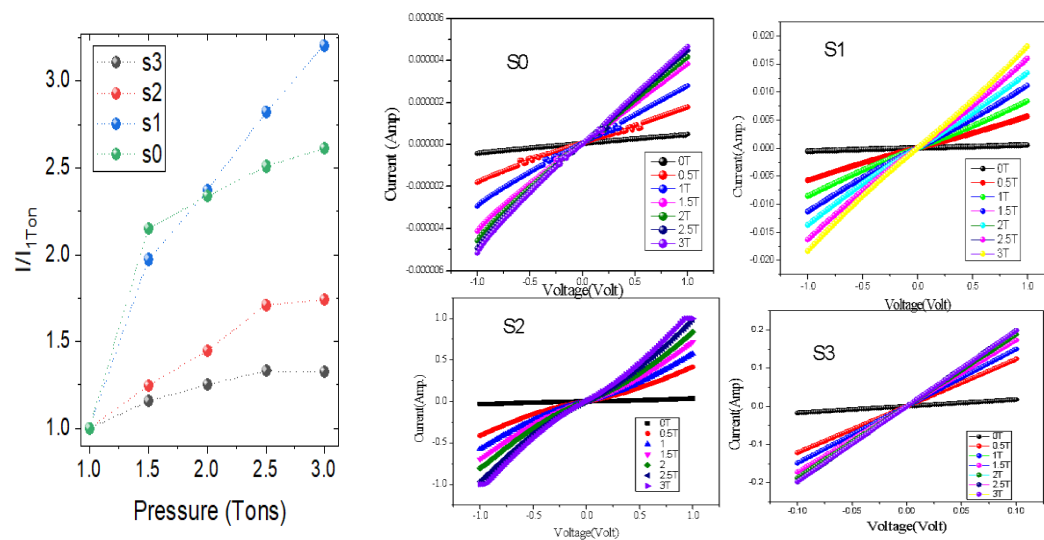


Figure 17 pressure vs current plots at different constant voltages.

In *S0*, *Li* is absent. Yet we observe an increase in the current when compared to the current observed at 1 ton pressure. The conductance seems to saturate at higher pressures. It implies that with increase of pressure the changes of electron clouds are favorable for the electron mobility in *S0* despite the very low current that was observed in this material. Hence, *Al* indeed helps to increase the free path of the carriers in this sample under pressure and helps increase the mobility of the carriers.

One needs to keep in mind that the extra oxygen that may be incorporated in the lattice may also play an important role in the reduced conductance of *S0* but may play a role in reduction of the free path between two collisions of the carriers. The conductance increases considerably with the introduction of the *Li* ions. This may be due to the incorporation of  $V_O$  which helps to generate more carriers and improves the free path providing a better mobility of the materials. The mobility seems to improve by reducing the hopping length of carriers and increasing the collision time, i.e. the free path. The interesting observation is the better conductivity of the *S2* samples than the *S3* sample at higher pressure. The *S3* sample does not contain  $Al^{3+}$  ions, and hence, a  $V_O$  compensation mechanism is absent in this sample. On the other hand, the *S2* sample has a larger population of  $Li^+$  ions which increases the number of carriers as well as might reduce the hopping distances of the carriers. On top of that, with the applied pressure these distances may be lessened thereby improving the conductivity. The optimization of the  $V_O$  population may have been obtained in this *S2* sample. In the *S3* sample the  $V_O$  may have increased to such a level that the lattice distortions have played a major role in increasing the free path thereby reducing the mobility.

### **3.8 Electroluminescent Analysis**

When a strong electric field is applied on a material, a considerable amount of current may flow through it. Depending on the amount of current flowing through the material the electrons can have a high energy which can excite electrons from the  $VB$  to higher states, including the conduction band ( $CB$ ) [95]. Hence,  $e-h$  pairs are produced which can readily recombine by emitting photons with energy equivalent to the difference between the energy levels occupied by the  $e-h$  pair. This phenomenon is known as electroluminescence ( $EL$ ), and is different from other types of luminescence excited by other types of energy sources like heat (incandescence), chemical energy (chemiluminescence), sonic energy (sonoluminescence), mechanical energy (mechanoluminescence), etc.. Phosphors are an example used in electroluminescent displays.

No, *EL* was observed for *S0* but a stable *EL* was observed for *S1*, *S2*, *S3* as dots distributed across the entire surface visible to the naked eyes. The observed *EL* is a continuous spectrum in the range 450-1100 nm and is spread over the same range for all  $Li^+$ -doped samples. The *EL* starts to show up at an applied voltage of  $\sim 6V$  and continues to increase with increase in the applied voltage [Figure 25]. The increments of *EL* intensity for the *S3* is shown [Figure 25]. The spectra consist of a prominent feature in the range of red light (700~775 nm), along with another lesser intense feature in the IR region of 860~930 nm. Hence, these materials are red light and IR radiators.

Sometimes the selection rules allow certain electronic transitions in a regular centrosymmetric structure. However, by doping different elements for example transition metals are alkaline metal some transition can be allowed. These transitions may correspond to sub-band gap nature. Most probably, the *EL* observed in these materials belong to such transitions which are induced by  $Li^+$ . Spin orbital coupling may break the parity due to a structural distortion which leads to lowering of the symmetry. Such transitions are reported thereby absorbing or emitting photons. In the UV-visible absorption spectra a strong feature is observed at  $\sim 1.7eV$  region corresponding to a transition of 720 nm wavelength along with another extremely weak feature in the region 1-1.5 eV which corresponds to  $\sim 900$  nm wavelength. A theoretical calculation needs to be done to find out a possible mechanism of these transitions. This work is a precursor to a future theoretical work related to the understanding of the details of all the transitions possible within the

bandgap.

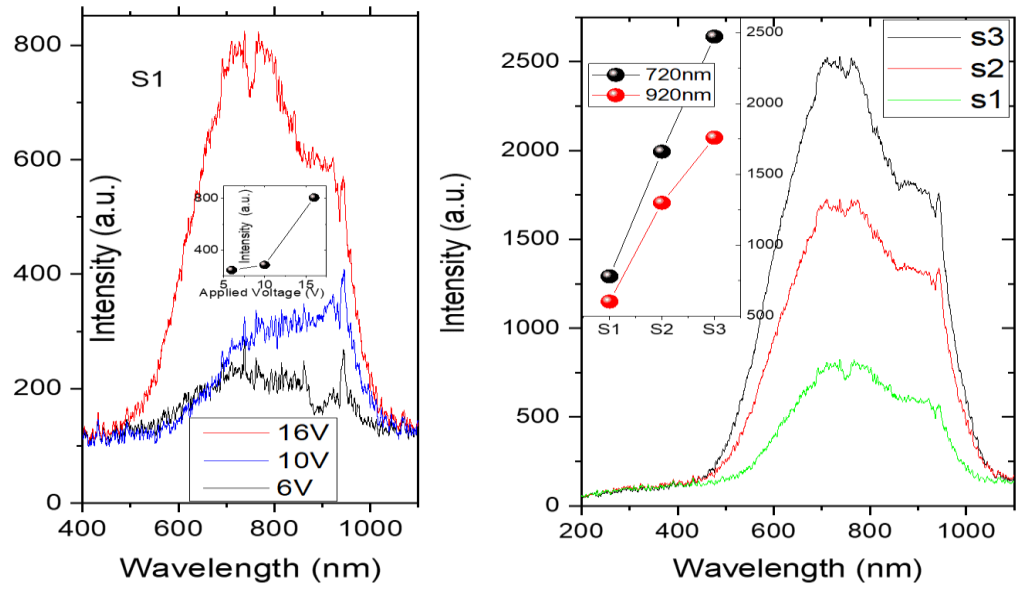


Figure 25 Electroluminescent spectra



Fig:-26 Electroluminescent spot

### 3.9 Summary of this chapter

*Solgel prepared  $Ni_{0.9844}(Al_xLi_{1-x})_{0.0156}$  nanoparticles revealed a cubic  $NiO$  structure of phase group (Fm-3m). The host cation being  $Ni^{2+}$ , the  $Al^{3+}$  doped system is an oxygen rich system due to the extra positive charge of  $Al^{3+}$  as compared to  $Ni^{2+}$ . Gradual substitution of  $Al^{3+}$  by  $Li^+$  in the  $Al^{3+}$ -doped  $NiO$  system reveals a transformation from an oxygen rich to an oxygen deprived lattice in the modified samples. This increases strain in the lattice upto the point where  $Al^{3+}$  is still present in the lattice. The  $Al^{3+}$  being completely removed, the  $Li^+$  manages to introduce a huge amount of oxygen vacancies which in turn releases the lattice strain due to the larger size of the  $Li^+$ -ion. The hybridization of the  $Li^+$  ion with the neighboring anions result in several new energy level creations inside the band gap which act as excitation centers and are revealed by absorption studies. Such levels contribute to electron hole pair formation and further recombination leading to strong red and IR electroluminescence. This luminescence increases with applied electric fields and with the amount of  $Li^+$  doping. On the other hand, the latent defects are sensitive to  $UV$  light and the electron hole pair formation and recombination can be associated with the adsorption-desorption processes at the surface. The photoresponse due to such processes decreases with  $Li^+$  doping. Hence, photostability increases with  $Li^+$  doping. The application of pressure was found to modify the electronic properties most probably due to modifications in the electronic clouds of molecular orbitals. Such modifications increase the conductive properties of the materials. The modifications in the electronic clouds can also be realized from the Localised Surface Plasmon Resonance features observed in the optoelectronic absorption studies.*

## Chapter 4

# Modified B site by Mn Doping, Structural, microstructural, and electronic studies of $ZnTi_{1-x}Mn_xO_3$ ceramics.

The polycrystalline  $ZnTi_{1-x}Mn_xO_3$  (for  $x = 0, 0.125, 0.25,$  and  $0.50$ ) are synthesized by modified sol-gel process[104]. The goal of this chapter is to look at the structural properties in depth. [105], surface morphology[106], vibrational[107] and optoelectronic[108] properties of  $Mn^{2+}$  doped  $ZnTiO_3$  ceramics. All the samples are prepared at  $500^\circ C-6h$  to observe the differing material qualities. To tune the structural and optical properties for various applications , Mn is doped in  $ZnTiO_3$ .

### 4.1 Synthesis:

Sol-gel processed polycrystalline  $ZnTi_{1-x}Mn_xO_3$  (for  $x = 0, 0.125, 0.25,$  and  $0.50$ )[hereafter called as S0,S1,S2, and S3] ceramics were prepared using zinc acetate (Alfa Aesar, purity 98.5%), titanium (IV) bis (ammonium lactate) hydroxide of 50% w/w aqueous solution, and manganese nitrate (99.7%). The reported samples were annealed at  $800^\circ C$  for 6hr.

### 4.2 X-ray diffraction analysis:

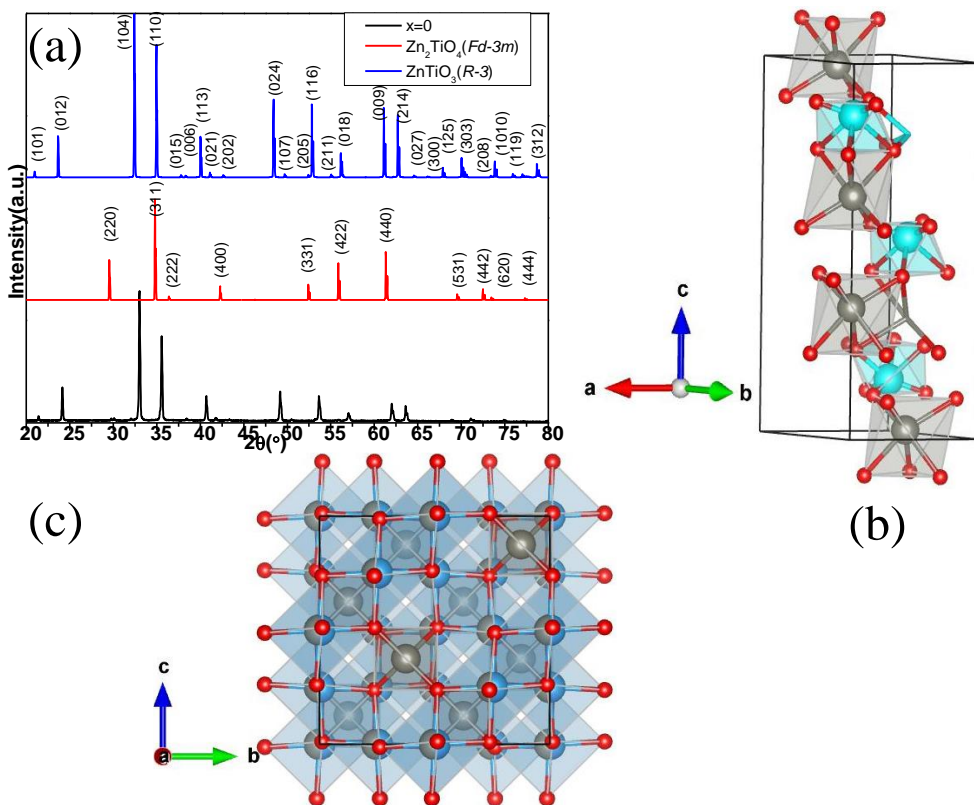


Figure 27(a) the XRD pattern of  $\text{ZnTi}_{1-x}\text{Mn}_x\text{O}_3$   $x=0, 0.125, 0.25, \text{ and } 0.50$  and (b-c) the zoomed view of one peak at  $2\theta = 35^\circ$ .

The Rietveld analysis was used to evaluate the obtained X-Ray diffraction patterns of all the prepared samples using the Full-Prof suite software. The goodness of fit ( $\chi^2$ ) values were obtained for all the samples from the mixed phase Rietveld refinement mentioned in Fig.31. The Rietveld refinement analysis suggested the presence of both  $\text{ZnTiO}_3$  ( $R-3$ ) and  $\text{Zn}_2\text{TiO}_4$  ( $Fd-3m$ ) phases in all the prepared samples confirming the formation of composite. The phase percentage of the  $\text{Zn}_2\text{TiO}_4$  ( $Fd-3m$ ) phase increased with increase in the Mn percentage.

Table 1 provides the phase percentage of both  $\text{ZnTiO}_3$  ( $R-3$ ) and  $\text{Zn}_2\text{TiO}_4$  ( $Fd-3m$ ) phase for all the samples. In the S0 sample there is a presence of 2%  $\text{Zn}_2\text{TiO}_4$  ( $Fd-3m$ ) phase which is a minor presence that is noticed from the peak at  $\sim 2\theta = 30^\circ$  which is due to the  $(220)$  reflection from  $\text{Zn}_2\text{TiO}_4$  ( $Fd-3m$ ). In the S0 sample, the intensity of the  $(220)$  peak is minimum and with an increase in the percentage of Mn doping the intensity of this peak increased because of the increase

in  $\text{Zn}_2\text{TiO}_4$  ( $Fd-3m$ ) phase. The S3 sample completely converted the  $\text{Zn}_2\text{TiO}_4$  to the  $\text{Zn}_2\text{TiO}_4$  ( $Fd-3m$ ) phase without any presence of  $\text{ZnTiO}_3$  ( $R-3$ ) phase. From Fig. 32(a) the cubic lattice parameters were found to be increasing for S1 but decreased for the S2 and S3 samples. The variation of the rhombohedral lattice parameters also increased with Mn-doping [Fig. 32(a)]. As the  $\text{Zn}_2\text{TiO}_4$  phase percentage increased to 77%, the cubic lattice parameters decreased while the rhombohedral lattice parameters increased continuously. It suggests that the rhombohedral lattice is expanding while the cubic lattice expanded from S0 to S2 sample and further contracted for S3 with Mn doping. The trend in both rhombohedral and cubic lattice parameters are in good agreement with the trend in strain with composition. The Williamson-Hall equation can be used to estimate lattice strain  $\epsilon$ , which is a measure of crystal flaws such as lattice dislocation, non-uniform lattice distortions is given as  $\epsilon = \frac{\beta}{4 \tan(\theta)}$ . It is evident from XRD analysis that the Mn doped samples prefer to be in the  $\text{Zn}_2\text{TiO}_4$  phase rather than the  $\text{ZnTiO}_3$  phase.

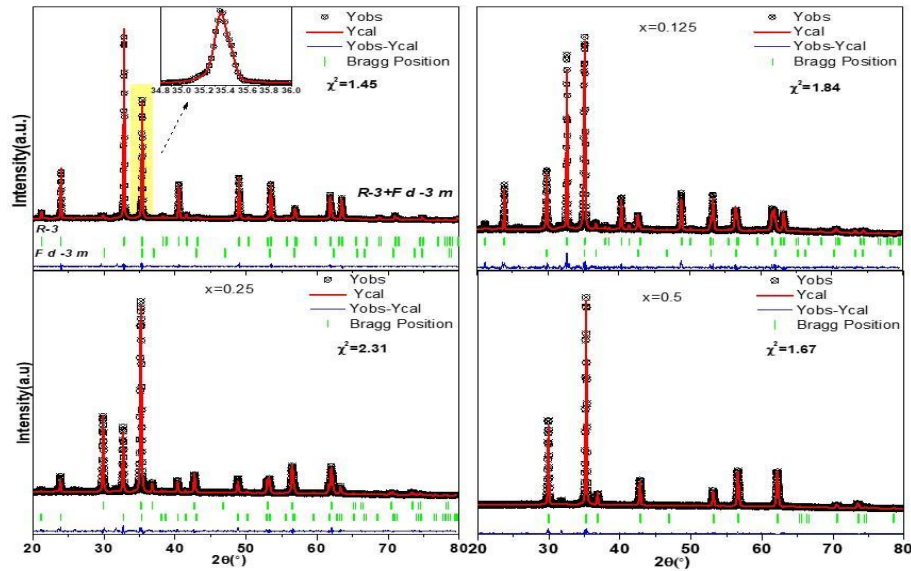


Figure 31 The Rietveld refinement of XRD data of  $\text{ZnTi}_{(1-x)}\text{Mn}_x\text{O}_3$  (a) S0 (b) S1 (c) S2 (d) S3.

So, it can be predicted that the Mn atom is in the mixed oxidation state i.e., mixed states of  $\text{Mn}^{3+}$  and  $\text{Mn}^{4+}$ . In the ideal Mn doped  $\text{ZnTiO}_3$  and  $\text{Zn}_2\text{TiO}_4$  phase

Mn is in  $Mn^{4+}$  state. The ionic radii of  $Mn^{3+}$  (high spin) is  $\sim 0.645\text{\AA}$  while the ionic radii of  $Mn^{4+}$  is  $0.53\text{\AA}$ . The ionic radii of  $Ti^{4+}$  is  $0.605\text{\AA}$ . From the structural analysis it was clear that the strain in the samples increased from S0 to S2 and decreased for the S3 sample. In the composite structures that are the S1 and S2 samples,  $Mn^{3+}$  is having more ionic radii than the  $Ti^{4+}$  which causes the unit cell to expand. But in the S3 sample, which is having pure  $Zn_2TiO_4$  phase, the Mn atom is in  $Mn^{4+}$  state as  $Mn^{4+}$  has lesser ionic radii than  $Ti^{4+}$  leading to the contraction of the unit cell.

Scherrer's formula can be used to estimate the average crystallite size,  $D$ , which is a measure of the size of a coherently diffracting domain, given as  $= \frac{K\lambda}{\beta \cos(\theta)}$ , where  $\lambda$  is the X-ray wavelength,  $\beta$  is the FWHM of the concerned peak, and  $\theta$  is the diffraction angle. The average crystallite size decreased from  $\sim 73$  nm for S0 to  $\sim 40$  nm for S2 and again increased to  $\sim 50$  nm for S3.

Composition (x)	Phase percent age of $ZnTiO_3$ (R-3)	Phase percent age of $Zn_2TiO_4$ (Fd-3m)	Rhombohedral Lattice parameters		Cubic Lattice parameters	Cell Volume ( $\text{\AA}^3$ )	
			$a_R=b_R$ ( $\text{\AA}$ )	$c_R$ ( $\text{\AA}$ )		$a=b=c$ ( $\text{\AA}$ )	$V_R$ ( $\text{\AA}^3$ )
0	98	2	5.074(3)	13.925(4)	8.426(2)	310.550(6)	598.24(2)
0.125	40	60	5.080(1)	13.941(3)	8.436(3)	311.609(1)	600.52(4)
0.25	23	77	5.092(2)	13.987(5)	8.462(2)	314.079(4)	605.95(6)
0.5	0	100	-	-	8.446(3)	-	602.68(2)

Table 1:- phase percentage ratio with concentration and atomic position.

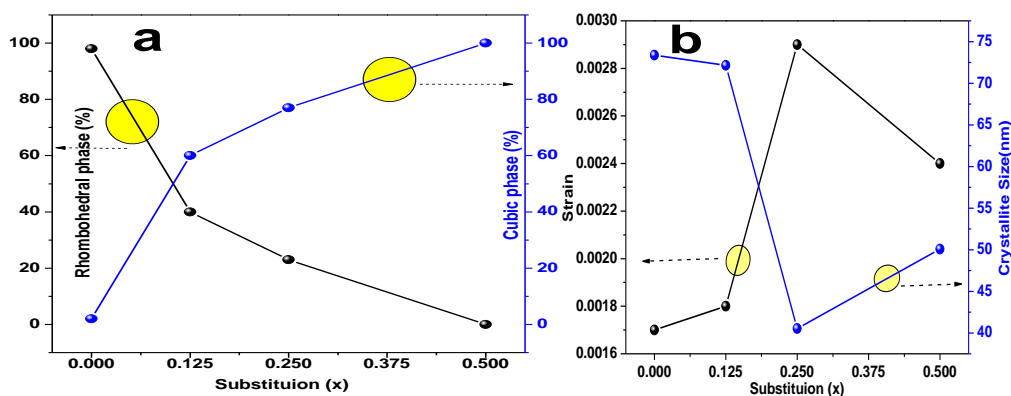


Figure 28(a) Percentage ratio of phase with substitution (b) the strain and crystallite size of ZnTi(1-x)Mn(x)O3 samples

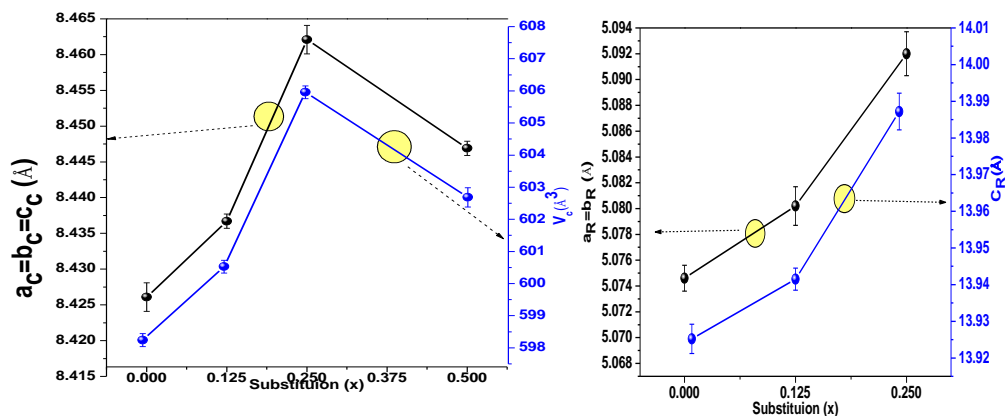


Figure 29 The lattice parameters variation with substitution.

To understand the structural transformation in detail, the bond length and bond angle analysis of all the compositions were done using VESTA software. The unit cells of both the rhombohedral and the cubic structure were drawn using the CIF files generated after doing the Rietveld refinement. It is well known that the ZnTiO<sub>3</sub> mostly exists in three structural forms. One is rhombohedral (*R*-3), second

is the cubic structure ( $Pm-3m$ ), and the third one is the perovskite form having ( $R3c$ ) space group. The most common structure among all is the rhombohedral ( $R-3$ ) structure which is also called ilmenite structure[110]. In the  $ZnTiO_3$  ilmenite ( $R-3$ ) structure, the Zn atom has co-ordination number six and Ti also has co-ordination number six. So, both the Ti and Zn atoms form  $TiO_6$  ( $BO_6$ ) and  $ZnO_6$  ( $AO_6$ ) octahedra, respectively. The same types of octahedra relate to edge sharing, while each type of octahedron shares one face with the other type in the adjacent layer, stacking alternatively along c-axis. Ilmenite has a hexagonal close-packed oxygen lattice with metal atoms taking up two-thirds of the available octahedral spaces. Each octahedron has three edges that connect to octahedra inside the layer, one face that connects to an octahedron of the second type of cation in the neighboring layer, and one face that connects to a vacant octahedral site. Out of six oxygen atoms in an octahedra, set of three oxygen atoms are shared by Ti and Zn atoms. Six A-O bonds can be divided into two sets as the set of three bonds are equal. One set is denoted as the A-Oa and the other one as A-Ob. The A-Oa set is the longer one while the A-Ob is the shorter one. Same observation was made for the B-O bonds as well. Both the long and short A-O bonds increased with increase in Mn substitution. The shorter bond angle is associated with the longer bond length and vice-versa. The shortest O-A-O bond angle decreased from  $73.63^\circ$  for S0 to  $72.16^\circ$  for S1 and again increased to  $76.67^\circ$  for S3. This kind of behavior of shortest O-A-O bond angle can be understood from the trend in long B-O bond length. In the ilmenite structure three oxygens (named as Oa) are common to both A and B site atoms through which A and B atoms are connected. The bond length of A-Oa and B-Oa are both longest while the other set of bond lengths are the shortest one. The longer B-Oa bond length also influences the shorter Oa-A-Oa bond angle and same with the long A-Oa bond length and short Oa-B-Oa bond angle. The longest B-O bond length decreased from  $2.076 \text{ \AA}$  for S0 to  $2.046 \text{ \AA}$  for S1 and again increased to  $2.167 \text{ \AA}$  for S2. But the shortest O-B-O bond angle associated with this bond length continuously decreased which is due to the net effect produced from both the B-O and A-O bond length. The shortest B-O bond length continuously decreased from  $1.845 \text{ \AA}$  for S0 to  $1.534 \text{ \AA}$  for S2. The longest Oa-B-Oa bond angle

associated with it also continuously increased from  $103.25^\circ$  for S0 to  $109.785^\circ$  for S2.

The  $\text{Zn}_2\text{TiO}_4$  shows the inverse spinel structure having  $\text{Fd-}3\text{m}$  (cubic)[111] space group. Similarly, cubic inverse spinel  $\text{Zn}_2\text{TiO}_4$  is composed of 56 sites represented as  $(\text{Zn}_8)^{\text{I}}(\text{Zn}_8\text{Ti}_8)^{\text{O}}\text{O}_{32}$ , where 8  $\text{Zn}^{2+}$  cations occupy tetrahedral sites, while other 8  $\text{Zn}^{2+}$  cations along with 8  $\text{Ti}^{4+}$  cations occupy the octahedral sites. The tetrahedra and octahedra are connected by one oxygen atom. In the cubic structure all the A-O bond lengths and bond angles in the tetrahedra are equal and all the B-O/A-O bond lengths and bond angles in the octahedra are equal. The A-O bond length increased from  $1.968\text{\AA}$  for S0 to  $2.009\text{\AA}$  for S2 and decreased to  $1.931\text{\AA}$  for S3. Such a trend in A-O bond length in the cubic structure is also responsible for the strain in the samples. The B-O-A bond angle decreased from  $126.52^\circ$  for S0 to  $121.2^\circ$  for S2 and increased to  $122.91$  for S3. This kind of change in this bond angle influenced the A-O bond length and so the lattice strain was also influenced. The B-O bond length increased from  $2.026\text{\AA}$  for S0 to  $2.029\text{\AA}$  for S1 and again decreased to  $2.018\text{\AA}$  for S2 and further increased to  $2.054\text{\AA}$  for S3. While the O-B-O bond angles increased from  $85.18^\circ$  for S0 to  $96^\circ$  for S2 and further decreased to  $93.36^\circ$  for S3.

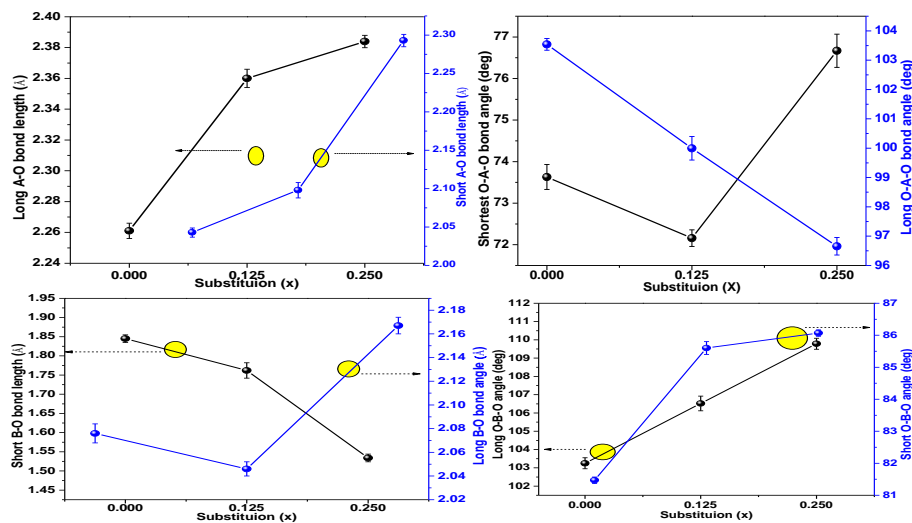


Figure 30 Bond angle variation with substitution.

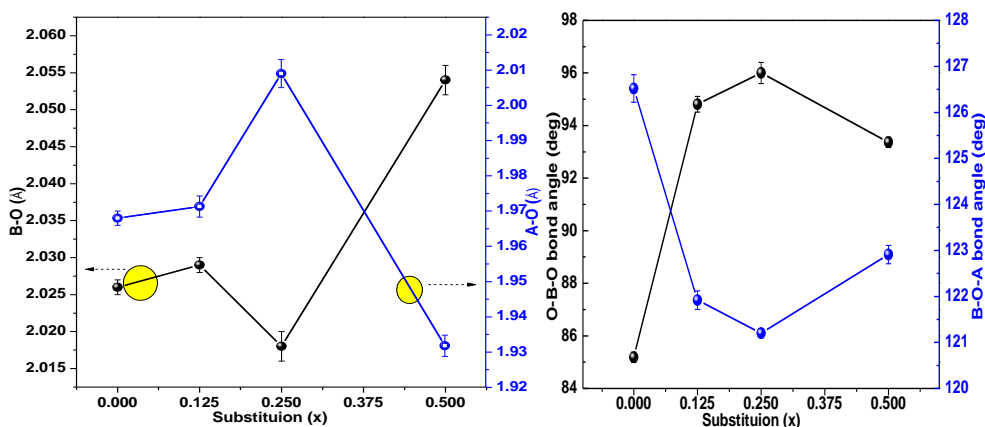


Figure 31 Bond angle variation with substitution.

### 4.3 Raman Spectroscopy:

The ilmenite structure of  $\text{ZnTiO}_3$  has R-3 space group, therefore the reducible representation of the Raman active modes is written as  $T_{\text{opt}} = 4A_g + 4^1E_g + 4^2E_g$  [9]. Out of the 12 modes three modes ( $A_g + ^1E_g + ^2E_g$ ) belong to the 6c Wyckoff position and 9 modes ( $3A_g + 3^1E_g + 3^2E_g$ ) belong to the 18f Wyckoff position. The  $\text{Zn}_2\text{TiO}_4$  stabilizes at Fd-3m space group, and the irreducible representation of the phonons is written as  $T_{\text{opt}} = A_{1g} + E_g + 2T_{2g} + T_{2g}$ . Out of these 5 Raman active modes one mode ( $T_{2g}$ ) belongs to 8a Wyckoff position, and four modes ( $A_{1g} + E_g + 2T_{2g}$ ) belong to the 32e Wyckoff position. The phonon modes were calculated for both the  $\text{ZnTiO}_3$  (R-3) and  $\text{Zn}_2\text{TiO}_4$  (Fd-3m) structures using the DFT calculation.

The Raman spectrum in dependence of the composition of ZTO samples at  $800^\circ\text{C}$  for a wide range of frequency 100-800  $\text{cm}^{-1}$  and carried out at room temperature shown in Figure 32.

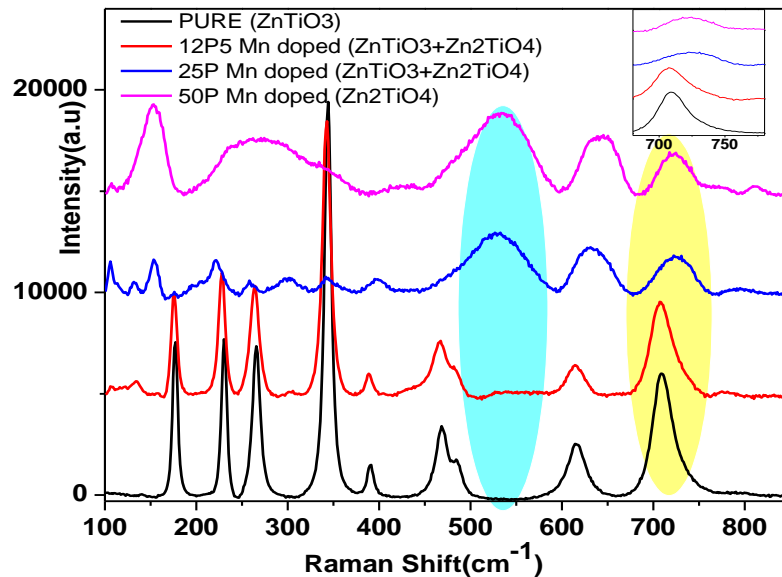


Figure 32 The Raman spectra of  $ZnTi(1-x)Mn(x)O_3$   $x=0, 0.125, 0.25$  and  $0.50$ .

A broad feature appears at lower frequencies due to the overlap of several Raman modes. These Raman modes are considerably broad (FWHM  $\sim \text{cm}^{-1}$  individually). This may be a consequence of the considerably increasing  $Zn_2TiO_4$  phase. ZTO shows different phase transitions when continuously increasing doping such as rhombohedral to cubic. From the figure, it was found that in cubic phase some Raman modes are merged.

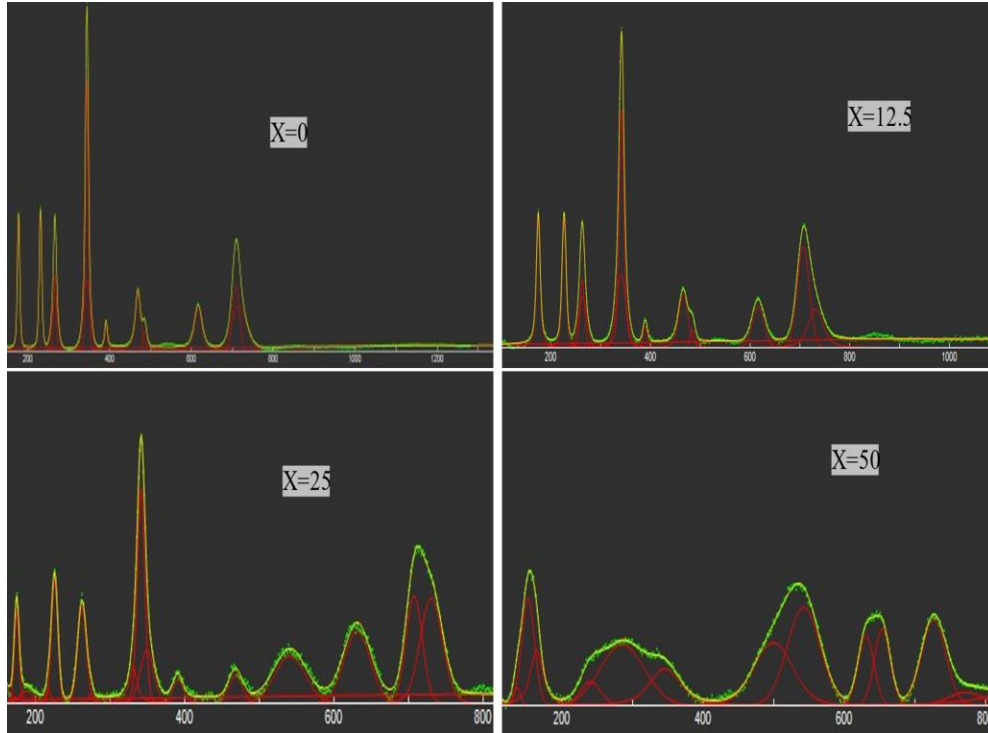


Figure 33 Raman fitted data of  $\text{ZnTi}(1-x)\text{Mn}(x)\text{O}_3$  samples.

#### 4.4 UV Vis spectroscopy analysis:

The DRS data was used to estimate the energy gap ( $E_g$ ) using the Tauc relation:  $\alpha h\nu = A (h\nu - E_g)^n$ , where  $A$  is a constant,  $n$  is an index which determines the type of transitions of the photon absorption process,  $\alpha$  is the absorption coefficient, and  $h\nu$  is the energy in eV[112]. The value of  $n$  varies from  $\frac{1}{2}$  (for direct transition) to 2 (for indirect transition)[113]. The DRS spectra was transformed to absorption spectra using the Kubelka-Munk function which is given by:  $F(R_\infty) = \frac{(1-R_\infty)^2}{2R_\infty}$ , where  $F(R_\infty)$  is the Kubelka-Munk function,  $R_\infty = \frac{R_{\text{sample}}}{R_{\text{standard}}}$ , where  $R_{\text{sample}}$  is the diffuse reflectance of the sample,  $R_{\text{standard}}$  is the diffuse reflectance of the non-absorbing standard sample[114].

It is known that the  $\text{ZnTiO}_3$  is an indirect band[115] gap while the  $\text{Zn}_2\text{TiO}_4$  is a direct band[116] gap semiconductor. Due to the formation of  $\text{ZnTiO}_3$  and  $\text{Zn}_2\text{TiO}_4$  composite in the S0, S1, and S2 samples two types of band gap were

observed in all these samples. The S3 sample is in the  $\text{Zn}_2\text{TiO}_4$  phase and shows only a direct band gap. The nature of band gap in all the samples are in good agreement with the presence of phase in respective samples. The direct band gap continuously decreased from 3.38 eV to 2.02 eV with increase in Mn doping. In case of indirect band gap, the band gap decreased from the 3.01 eV for S0 to 1.65 eV for S2. In the S1 and S2 samples, two linear regions were observed in the indirect band plot. But, in the undoped Mn sample only single linear region was observed. The creation of an octahedral complex can explain such observations in the S1 and S2 samples. The origin of band gaps in these types of structures are due to the Ti 3d and O 2p. The Mn atom is being substituted in the Ti site.  $\text{Mn}^{3+}$  and  $\text{Mn}^{4+}$  are having electronic configuration  $[\text{Ar}] 3d^4$  and  $[\text{Ar}] 3d^3$ , respectively. In the octahedral crystal field, the 3d orbital is split into two  $e_g$  orbitals and three  $t_{2g}$  orbitals. This field makes  $e_g$  evolve into one high energy state ( $d_{x^2-y^2}$ ) and one low energy state ( $d_z^2$ ), and simultaneously  $t_{2g}$  evolve into one high energy state ( $d_{xy}$ ) and two low energy states ( $d_{yz}$  and  $d_{zx}$ ). Hence, with the addition of Mn ions, the 3d state is present between conduction band and valence band. The low indirect  $E_g$  is attributed to the interband transition from the  $d_z^2$  state to the state ( $d_{x^2-y^2}$ ) and the higher one is due to the transition from O 2p to Ti 3d. Urbach energy was investigated to better understand the influence of doping on lattice disorder. Crystal lattice disorder gives rise to localized electronic states very close to the band edges and can be calculated from the Urbach energy,  $E_U$ , using the relation  $\alpha = \alpha_0 e^{\frac{hv}{E_U}}$ , where " $\alpha_0$ " is a crystal parameter [117]. These localized electronic states being close to the band edges appear as an exponential tail of the absorption coefficient curve. The Urbach energy increased with Mn doping which shows increase in disorders in the lattice. Such increase in disorder is due to the compositional fluctuations in the samples.

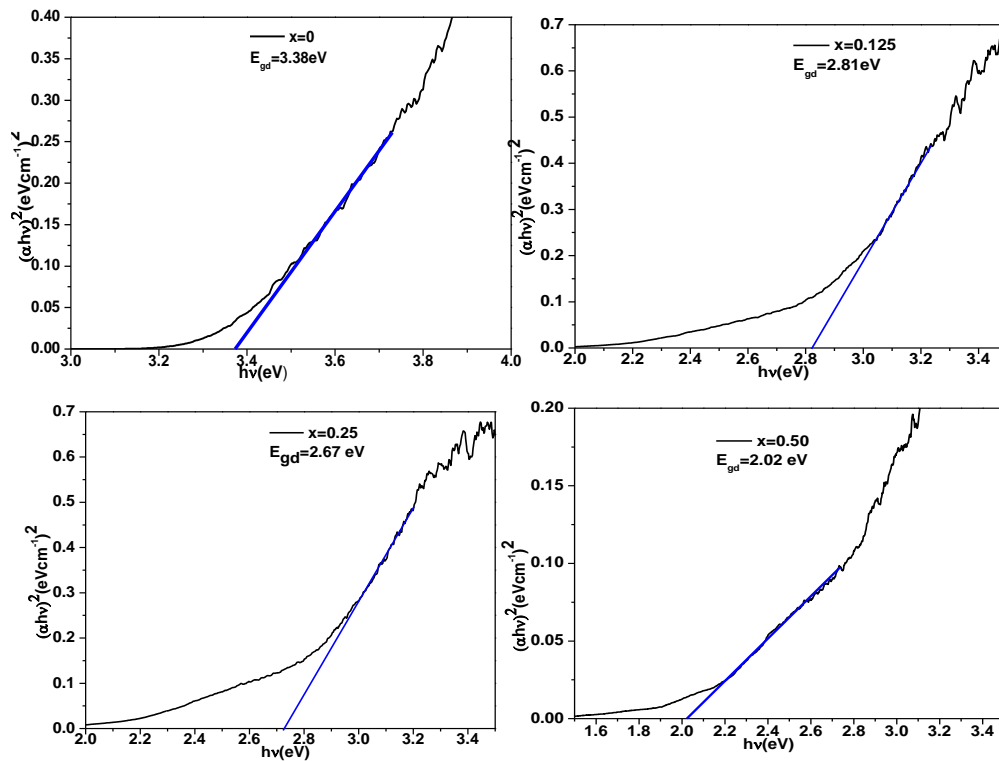


Figure 34 The band-edge from the UV-vis spectra ZnTi(1-x)Mn(x)O3 samples.

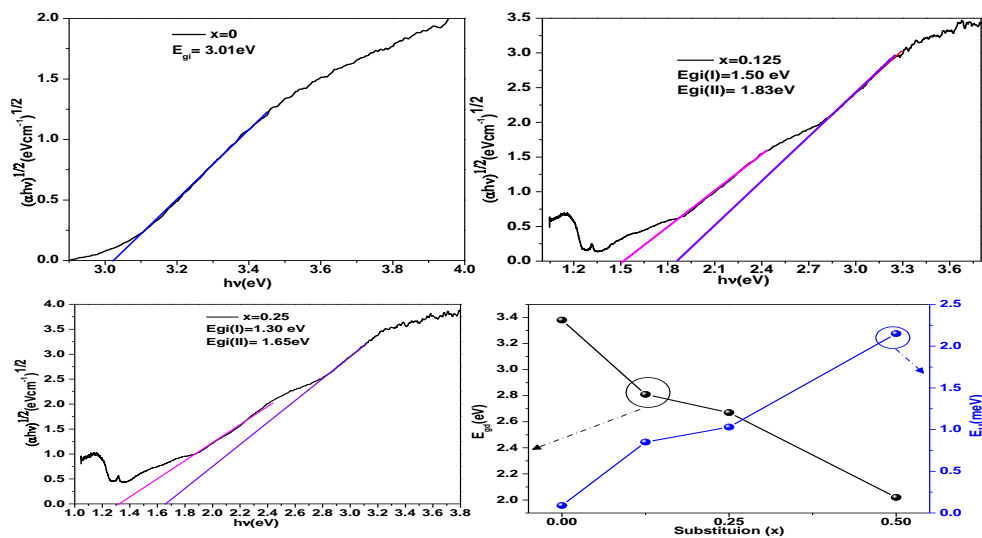


Figure 35 Decreases the electronic band gap with substitution.

## 4.5 Pressure dependent I-V Characteristics:

The pressure dependent (0-3 ton/mm<sup>2</sup>) I-V characteristics of all the prepared samples were studied. The pressure vs current plots at different constant voltages (1V, 2V, 5V, and 10 V) shows that the current value increased with increase in pressure value [Fig. 40]. Note these results were repeatable and the experiment was performed in several iterations on the same sample followed by similar runs on other specimens of the same composition. This justifies the fact that the pressure promotes the electron flow and increases the conductivity of the materials. In addition to the above observation, it was observed that the current increased with Mn-doping. This is in agreement with the band gap analysis. The reason for such increase of conduction may also be the rise or charge carriers, which can be confirmed from Hall effect measurements. The experiment is to be done in the near future. Unfortunately, in this report the results could not be reported to confirm the conductivity aspect of the materials. The maximum current flow for the S3 sample suggests that the presence of the direct band is stimulating the easy flow of electrons to the conduction band.

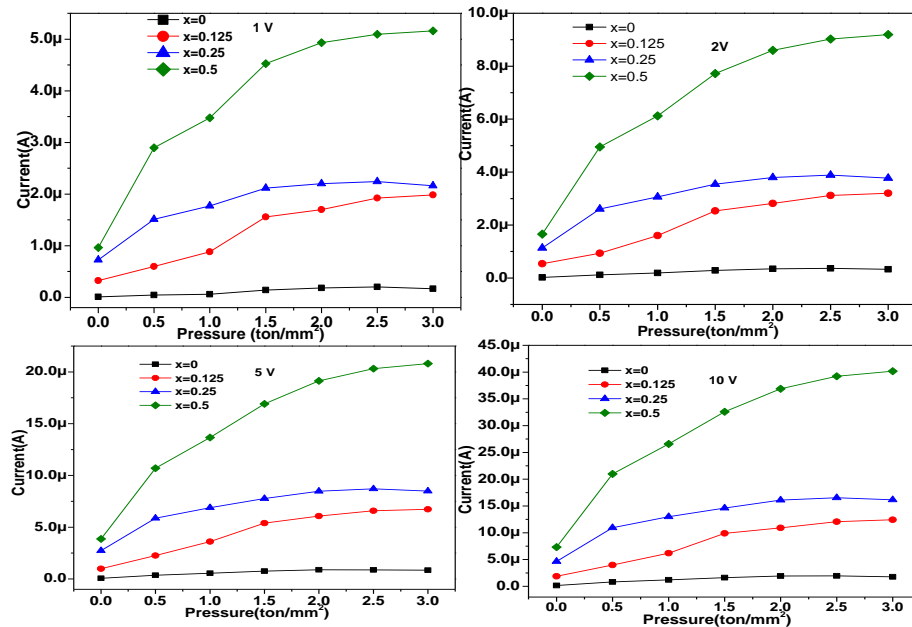


Figure 36 Pressure Vs Current plot at (a) 1 V (b) 2V (c) 5V (d) 10 V

## 4.6 Conclusions:

Sol-gel synthesis was used to make the Mn-doped ZnTiO<sub>3</sub> samples, which were then calcined. The increase in the Zn<sub>2</sub>TiO<sub>4</sub> (*Fd-3m*) phase with Mn doping was confirmed from the structural analysis using Rietveld refinement. UV-Vis spectroscopy research revealed a decrease in both direct and indirect band gap. Only an indirect band gap present in x=0.5 (S3) composition is in well agreement with the structural analysis. The increase in the current value with Mn doping was observed from the pressure dependent I-V characteristics.

## Summary

The key findings of this thesis work are as follows:

- Ni<sub>0.9844</sub>(Al<sub>x</sub>Li<sub>1-x</sub>)<sub>0.0156</sub>O: In Ni<sub>0.9844</sub>(Al<sub>x</sub>Li<sub>1-x</sub>)<sub>0.0156</sub>O lattice parameters  $a=b=c$  first increase for S0,S1,S2 and thereafter decrease gradually for S3. XRD and Raman studies revealed no secondary or clustered phases.
- ZnTiMnO<sub>3</sub>: The samples of Mn-doped ZnTiO<sub>3</sub> were made using a sol-gel method and then calcined. The increase in the Zn<sub>2</sub>TiO<sub>4</sub> (*Fd-3m*) phase with Mn doping was confirmed from the structural analysis using Rietveld refinement. UV-Vis spectroscopy research revealed a decrease in both direct and indirect band gap. There is only an indirect band gap presence in x=0.5 (S3) composition that is in well agreement with the structural analysis. The increase in the current value with Mn doping was observed from the pressure dependent I-V characteristics.

## Chapter 5

# Conclusions and Scope for Future Work

### Contribution of the thesis

The notable contribution of the thesis in understanding the structure, local structure, and electronic properties of Al/Li-doped NiO, and ZnTiMnO<sub>3</sub> samples is given below:

- A large enhancement in electric properties in antiferromagnet NiO is achieved with simultaneous small substitution Li for Ni site.
- The increase in the Zn<sub>2</sub>TiO<sub>4</sub> (*Fd-3m*) phase with Mn doping in ZnTiO<sub>3</sub>. The adopted methodology for the synthesis and investigation of dielectric properties can be of importance to the perovskite research community.
- This thesis provides evidence that methodology for the synthesis of Zn<sub>2</sub>TiO<sub>4</sub> is an important factor.
- In this work, it is also proved that a slightly increased Li doping concentration in NiO can result in a more conducting state compared to Al doped NiO.
- The bandgap and electric properties can be engineered by tuning the B-site of ZnTiO<sub>3</sub> as per the requirement of the spintronic industry. Similar in NiO.

### Future directions

The present work was focused on examining the structure-correlated properties and electric properties of perovskites and simple oxide. The research outcome of the thesis can be expanded to the next level.

- To confirm B-site ordering in ZnTiO<sub>3</sub>, a combination of magnetic, electron energy-loss spectroscopy (EELS), and scanning transmission electron microscopy (STEM) experiments are required.
- Effect of  $Li^{1+}/Al^{3+}$  can be investigated on the spin- phonon coupling in NiO

compounds. NiO can be further explored as a new solar cell.

- ZnTiMnO<sub>3</sub> is supposed to exhibit a phase transition at higher doping and high temperature; therefore, a combined temperature dependent dielectric and Raman studies may be performed to examine the phase transformation in these kinds of perovskites.
- Magnetodielectric properties may be explored in the future.
- There are a lot of scopes to investigate the magneto transport and magnetocaloric properties of these perovskites in the bulk as well as in single crystal or in thin films.
- In the future, thin films can be prepared from the bulk samples, which may yield better physical properties. The issues of anesite or local disorders may be avoided to explore them for direct application in spintronic industry.

**Reference:-**

- [1]. Tiwari J. N., Tiwari R. N., Kim K. S. (2012), Zero-dimensional, one-dimensional, two-dimensional, and three-dimensional nanostructured materials for advanced electrochemical energy devices, *Prog. Mater. Sci.*, 57, 724-803 (DOI: <https://doi.org/10.1016/j.pmatsci.2011.08.003>)
- [2]. Barth S., Hernandez-Ramirez F., Holmes J. D., Romano-Rodriguez A. (2010), Synthesis and applications of one-dimensional semiconductors, *Prog. Mater. Sci.*, 55, 563-627 (DOI: <https://doi.org/10.1016/j.pmatsci.2010.02.001>)
- [3]. Yang M., He J., Hu X., Yan C., Cheng Z. (2011), CuO Nanostructures as Quartz Crystal Microbalance Sensing Layers for Detection of Trace Hydrogen Cyanide Gas, *Environ. Sci. Technol.*, 45, 6088-6094 (DOI: 10.1021/es201121w)
- [4]. Sui R., Charpentier P. (2012), Synthesis of Metal Oxide Nanostructures by Direct Sol–Gel Chemistry in Supercritical Fluids, *Chem. Rev.*, 112, 3057-3082 (DOI: 10.1021/cr2000465)
- [5]. Fernández-García M., Martínez-Arias A., Hanson J. C., Rodriguez J. A. (2004), Nanostructured Oxides in Chemistry: Characterization and Properties, *Chem. Rev.*, 104, 4063-4104 (DOI: 10.1021/cr030032f)
- [6]. O'Regan B., Grätzel M. (1991), A low-cost, high-efficiency solar cell based on dye-sensitized colloidal TiO<sub>2</sub> films, *Nature*, 353, 737 (DOI: 10.1038/353737a0)
- [7]. Bjoerksten U., Moser J., Graetzel M. (1994), Photoelectrochemical Studies on Nanocrystalline Hematite Films, *Chem. Mater.*, 6, 858-863 (DOI: 10.1021/cm00042a026)
- [8]. Olsen J. S., Gerward L., Jiang J. Z. (1999), On the rutile/ $\alpha$ -PbO<sub>2</sub>-type phase boundary of TiO<sub>2</sub>, *J. Phys. Chem. Solids*, 60, 229-233 (DOI: [https://doi.org/10.1016/S0022-3697\(98\)00274-1](https://doi.org/10.1016/S0022-3697(98)00274-1))

[9]. Wang J., Chen R., Xiang L., Komarneni S. (2018), Synthesis, properties and applications of ZnO nanomaterials with oxygen vacancies: A review, *Ceram. Int.*, 44, 7357-7377 (DOI: <https://doi.org/10.1016/j.ceramint.2018.02.013>)

[10]. El-Kemary M., Nagy N., El-Mehasseb I. (2013), Nickel oxide nanoparticles: Synthesis and spectral studies of interactions with glucose, *Mater. Sci. Semicond. Process.*, 16, 1747-1752 (DOI: <https://doi.org/10.1016/j.mssp.2013.05.018>)

[11]. Raj A. S. A., Biju V. (2017), Nanostructured CuO: Facile synthesis, optical absorption and defect dependent electrical conductivity, *Mater. Sci. Semicond. Process.*, 68, 38-47 (DOI: <https://doi.org/10.1016/j.mssp.2017.05.008>)

[12]. Taheri R. 2015; Electrical conductivity of CuO nanofluids, Vol. 6, p 77-81.

Gao D., Zhang J., Zhu J., Qi J., Zhang Z., Sui W., Shi H., Xue D. (2010), Vacancy-Mediated Magnetism in Pure Copper Oxide Nanoparticles, *Nanoscale Res. Lett.*, 5, 769 (DOI: [10.1007/s11671-010-9555-8](https://doi.org/10.1007/s11671-010-9555-8))

[13]. Marabelli F., Parravicini G. B., Salghetti-Drioli F. (1995), Optical gap of CuO, *Phys. Rev. B*, 52, 1433-1436 (DOI: [10.1103/PhysRevB.52.1433](https://doi.org/10.1103/PhysRevB.52.1433))

[15]. Yang, H.; Tao, Q.; Zhang, X.; Tang, A.; Ouyang, J. Solid-state synthesis, and electrochemical property of SnO<sub>2</sub>-NiO nanomaterials. *J. Alloys Compd.* 2008, 459, 98. [CrossRef]

[16]. 2. Fujii, E.; Tomozawa, A.; Torii, H.; Takayama, R. Preferred orientations of NiO films prepared by plasma enhanced metal organic chemical vapor deposition. *J. Appl. Phys.* 1996, 35, 328. [CrossRef]

[17]. Sato, H.; Minami, T.; Takata, S.; Yamada, T. Transparent conducting p-type NiO thin films prepared by magnetron sputtering. *Thin Solid Films* 1993, 236, 27. [CrossRef]

[18]. Kitao, M.; Izawa, K.; Urabe, K.; Komatsu, T.; Kuwano, S.; Yamada, S. Preparation, and electrochromic properties of RF-sputtered NiO<sub>x</sub> films prepared in Ar/O<sub>2</sub>/H<sub>2</sub> atmosphere. *J. Appl. Phys.* 1994, 33, 6656. [CrossRef]

- [19]. Kumagai, H.; Matsumoto, M.; Toyoda, K.; Obara, M. Preparation and characteristics of nickel oxide thin film by controlled growth with sequential surface chemical reactions. *J. Mater. Sci. Lett.* 1996, 15, 1081. [CrossRef]
- [20]. Nikolay K. Kotsev 1 and Luba I. Ilieva *Catalysis Letters* 18 (1993) 173-176
- [21]. ARDELEAN *Modern Physics Letters B*, Vol. 15, No. 16 (2001) 523–527
- [22]. F. Fiévet, P. Germi, F. de Bergevin and M. Figlarz *J. Appl. Cryst.* (1979). 12, 387-394
- [23]. K. Anandan n , V. RajendranK. Anandan, V. Rajendran / *Materials Science in Semiconductor Processing* 14 (2011) 43–47
- [24]. Hao-Long Chena,\* , Yang-Ming Lub , Weng-Sing Hwanga *Surface & Coatings Technology* 198 (2005) 138 – 142
- [25]. Michael Nolan,1,a) Run Long,2 Niall J. English,2,b) and Damian A. Mooney2 *THE JOURNAL OF CHEMICAL PHYSICS* 134, 224703 (2011)
- [26]. S. L. Dudarev, G. A. Botton, S. Y. Savarsov, C. J. Humphreys, and A. P. Sutton, *Phys. Rev. B* 57, 1505 (1998).
- [27]. V. I. Anisimov, J. Zaanen, and O. K. Andersen, *Phys. Rev. B* 44, 943 (1991)
- [28]. . K. Anandan n , V. RajendranK. Anandan, V. Rajendran / *Materials Science in Semiconductor Processing* 14 (2011) 43–47
- [29]. . Hao-Long Chena,\* , Yang-Ming Lub , Weng-Sing Hwanga *Surface & Coatings Technology* 198 (2005) 138 – 142
- [30]. Ashish Chhaganlal Gandhi 1,2 ID and Sheng Yun Wu 1, *Nanomaterials* 2017, 7, 231; doi:10.3390/nano7080231
- [31]. Ashish Chhaganlal Gandhi 1,2 ID and Sheng Yun Wu 1, *Nanomaterials* 2017, 7, 231; doi:10.3390/nano7080231

[32]. Wang W., Wang L., Shi H., Liang Y. (2012), A room temperature chemical route for large scale synthesis of sub-15 nm ultralong CuO nanowires with strong size effect and enhanced photocatalytic activity, *CrystEngComm*, 14, 5914-5922 (DOI: 10.1039/C2CE25666E).

[33]. Park J., Joo J., Kwon S. G., Jang Y., Hyeon T. (2007), Synthesis of Monodisperse Spherical Nanocrystals, *Angewandte Chemie International Edition*, 46, 4630-4660 (DOI: doi:10.1002/anie.200603148)

[34]. Serin T., Yildiz A., Horzum Şahin Ş., Serin N. (2011), Extraction of important electrical parameters of CuO, *Physica B*, 406, 575-578 (DOI: <https://doi.org/10.1016/j.physb.2010.11.044>)

[35]. Xie, Y.; Lu, K.; Duan, J.; Jiang, Y.; Hu, L.; Liu, T.; Zhou, Y.; Hu, B. Enhancing Photovoltaic Performance of Inverted Planar Perovskite Solar Cells by Cobalt-Doped Nickel Oxide Hole Transport Layer. *ACS Appl. Mater. Interfaces* 2018, 10, 14153–14159. [CrossRef]

[36]. Ashique Kotta and Hyung Kee Seo *Appl. Sci.* 2020, 10, 5415; doi:10.3390/app10165415

[37]. A. Madhavi G. S. Harish P. Sreedhara Reddy ISSN (online): 2349-784X (IJSTE/ Volume 2 / Issue 11 / 127)

[38]. Mari Napari<sup>1,2</sup> | Tahmida N. Huq<sup>1</sup> | Robert L. Z. Hoye<sup>1,3</sup> | Judith L. MacManus-Driscoll DOI: 10.1002/inf2.12146

[39]. A. Diallo , K. Kaviyarasua, S. Ndiaye, B. M. Mothudia, A. Ishaq, V. Rajendran and M. Maazaa VOL. 11, NO. 2, 166–175 <https://doi.org/10.1080/17518253.2018.1447604>

[40]. Diego Di Girolamo , Francesco Di Giacomo <sup>c</sup>, Fabio Matteocci <sup>c</sup>, Andrea Giacomo Abate DOI: 10.1039/D0SC02859B (Minireview) *Chem. Sci.*, 2020, 11, 7746-7759

- [41]. Se-W. Parka , Jeong-M. Choia , Eugene Kimb , Seongil Ima, S.-W. Park et al. / Applied Surface Science 244 (2005) 439–443
- [42]. Shuyi Liu†, Rui Liu†, Ying Chen†, Szuheng Ho†, Jong H. Kim†, and Franky So 10.1021/cm501898y
- [43]. J. A. Dawson,a) Y. Guo, and J. Robertson APPLIED PHYSICS LETTERS 107, 122110 (2015)
- [44]. Adawiya J. Haider a,\*, Riyad Al- Anbari b, Hiba M. Sami b, Mohammed J. Haider j m a t e r r e s t e c h n o l . 2 0 1 9 ; 8 ( 3 ) : 2 8 0 2 – 2 8 0 8
- [45]. Martha Ramesh Martha Purna Chander Rao and Sambandam Anandan Hosakoppa Nagaraja r. Res., Vol. 33, No. 5, Mar 14, 2018 <https://www.cambridge.org/core/terms>. <https://doi.org/10.1557/jmr.2018.30> D
- [46]. Jiang J, Li Y, Liu J, Huang X, Yuan C, Lou XWD (2012 Adv Mater 24:5166–5180. <https://doi.org/10.1002/adma.201202146>
- [47]. Lai C-H, Lu M-Y, Chen L-J (2012 J Mater Chem 22:19–30. <https://doi.org/10.1039/C1JM13879K>
- [48]. Wang B, Chen JS, Bin WH et al (2011) J Am Chem Soc 133:17146–17148. <https://doi.org/10.1021/ja208346s>
- [49]. Matsumiya M., Qiu F., Shin W., Izu N., Murayama N., Kanzaki S., “Thin-film Li-doped NiO for thermoelectric hydrogen gas sensor”, Thin Solid Films, 419(1-2), pp.213-217, 2002.
- [50]. So J.-Y., Lee C.-H., Kim J.-E., Kim H.-J., Jun J., Bae W.-G. (2018), Hierarchically Nanostructured CuO–Cu Current Collector Fabricated by Hybrid Methods for Developed Li-Ion Batteries, Materials, 11, 1018) [51]. Philip J., Shima P. D., Raj B. (2008), Nanofluid with tunable thermal properties, Appl. Phys. Lett., 92, 043108 (DOI: 10.1063/1.2838304)

- [52]. Hyeon T. (2003), Chemical synthesis of magnetic nanoparticles, *ChemComm.*, 927-934 (DOI: 10.1039/B207789B)
- [53]. Kralj S., Rojnik M., Kos J., Makovec D. (2013), Targeting EGFR-overexpressed A431 cells with EGF-labeled silica-coated magnetic nanoparticles, *J. Nanoparticle Res.*, 15, 1666 (DOI: 10.1007/s11051-013-1666-6)
- [54]. Mahendran V., Philip J. (2012), Nanofluid based optical sensor for rapid visual inspection of defects in ferromagnetic materials, *Appl. Phys. Lett.*, 100, 073104 (DOI: 10.1063/1.3684969)
- [55]. Mornet S., Vasseur S., Grasset F., Veverka P., Goglio G., Demourgues A., Portier J., Pollert E., Duguet E. (2006), Magnetic nanoparticle design for medical applications, *Prog. Solid State Chem.*, 34, 237-247 (DOI:<https://doi.org/10.1016/j.progsolidstchem.2005.11.010>)
- [56]. Scarberry K. E., Dickerson E. B., McDonald J. F., Zhang Z. J. (2008), Magnetic Nanoparticle–Peptide Conjugates for in Vitro and in Vivo Targeting and Extraction of Cancer Cells, *J. Am. Chem. Soc.*, 130, 10258-10262 (DOI: 10.1021/ja801969b)
- [57] V. R. Boinapally, “Computational study of structural and electrical properties of methylammonium lead iodide perovskite,” University of Toledo, 2015.
- [58] B. ORAYECH, “Study of Crystal Structures and Phase Transitions in Perovskite-Type Oxides Using Powder-Diffraction Techniques and Symmetry-Mode Analysis.”
- [59] J. Sunarso, S. S. Hashim, N. Zhu, and W. Zhou, “Perovskite oxides applications in high temperature oxygen separation, solid oxide fuel cell and membrane reactor: a review,” *Prog. Energy Combust. Sci.*, vol. 61, pp. 57–77, 2017.

- [60] J. Yi, J. Brendt, M. Schroeder, and M. Martin, "Oxygen permeation and oxidation states of transition metals in (Fe, Nb)-doped  $\text{BaCoO}_{3-\delta}$  perovskites," *J. Membr. Sci.*, vol. 387, pp. 17–23, 2012.
- [61] M. S. Haluska and S. T. Misture, "Crystal structure refinements of the three-layer Aurivillius ceramics  $\text{Bi}_2\text{Sr}_{2-x}\text{A}_x\text{Nb}_2\text{TiO}_{12}$  (A= Ca, Ba, x= 0, 0.5, 1) using combined X-ray and neutron powder diffraction," *J. Solid State Chem.*, vol. 177, no. 6, pp. 1965–1975, 2004.
- [62] J. Suntivich, H. A. Gasteiger, N. Yabuuchi, H. Nakanishi, J. B. Goodenough, and Y. Shao-Horn, "Design principles for oxygen-reduction activity on perovskite oxide catalysts for fuel cells and metal–air batteries," *Nat. Chem.*, vol. 3, no. 7, pp. 546–550, 2011.
- [63]. Z. Liu, A. R. Paterson, H. Wu, P. Gao, W. Ren, and Z.-G. Ye, "Synthesis, structure and piezo-/ferroelectric properties of a novel bismuth-containing ternary complex perovskite solid solution," *J. Mater. Chem. C*, vol. 5, no. 16, pp. 3916–3923, 2017.
- [64] OSAMU YAMAGUCHI,\* MASAMI MOR~MI, HIDENAO KAWABATA, AND K~YOSHI SHIMIZU *J. Am. Ceram. SOC.*, 70 151 C-97-C-98 (1987)
- [65]. "T. Kuho, M. Kato, M. Mitarai, and K. Uchida, "Solid-State Reaction of the  $\text{TiO}_2$ -ZnO System," *Kogyo Kagaku Zasshi*, 66 [4] 403-407 (1963).
- [66]. A. I. Sheinkman, F. P. Sheinkman, I. P. Dobrovol'skii, and G. R. Zvyagina, "Phase Formation Sequence during the Reaction of Zinc Oxide with Titanium Dioxide," *Izv. Akad. Nauk SSSR, Neorg. Mater.*, 13 IS] 1447-50 (1977)
- [67] D. I. Woodward and I. M. Reaney, "Electron diffraction of tilted perovskites," *Acta Crystallogr. B*, vol. 61, no. 4, pp. 387–399, 2005.
- [68] A. Mishra and S. Bhattacharjee, "Effect of A-or B-site doping of perovskite calcium manganite on structure, resistivity, and thermoelectric properties," *J. Am. Ceram. Soc.*, vol. 100, no. 10, pp. 4945–4953, 2017.

- [69] S. Stølen, E. Bakken, and C. E. Mohn, “Oxygen-deficient perovskites: linking structure, energetics and ion transport,” *Phys. Chem. Chem. Phys.*, vol. 8, no. 4, pp. 429–447, 2006.
- [70] W.-J. Yin, B. Weng, J. Ge, Q. Sun, Z. Li, and Y. Yan, “Oxide perovskites, double perovskites and derivatives for electrocatalysis, photocatalysis, and photovoltaics,” *Energy Environ. Sci.*, vol. 12, no. 2, pp. 442–462, 2019.
- [71]. Hodeau J.-L., Guinebretiere R. (2007), Crystallography: past and present, *Appl. Phys. A*, 89, 813-823 (DOI: 10.1007/s00339-007-4223-2)
- [72]. Bryan R. (1993), Fundamentals of crystallography. IUCr Texts on Crystallography No. 2 by C. Giacovazzo, H. L. Monaco, D. Viterbo, F. Scordari, G. Gilli, G. Zanotti and M. Catti, *Acta Crystallogr., Sect. A: Found. Crystallogr.*, 49, 373-374 (DOI: doi:10.1107/S0108767392012285)
- [73]. Carvajal J. (1990), FULLPROF: A Program for Rietveld Refinement and Pattern Matching Analysis, Abstracts of the Satellite Meeting on Powder Diffraction of the XV Congress of the IUCr, (DOI: citeulike-article-id:1840305)
- [74]. Rietveld H. (1969), A profile refinement method for nuclear and magnetic structures, *J. Appl. Crystallogr.*, 2, 65-71 (DOI: doi:10.1107/S0021889869006558)
- [75]. Lercher J. A., Jentys A. (2007); Chapter 13 - Infrared and Raman Spectroscopy for Characterizing Zeolites. In *Studies in Surface Science and Catalysis*; Čejka, J.; van Bekkum, H.; Corma, A.; Schüth, F., Eds.; Elsevier: pp 435-476.
- [76]. Long D. A. (2005), *Introductory Raman Spectroscopy*. John R. Ferraro, Kazuo Nakamoto and Chris W. Brown. Academic Press, Amsterdam, Second Edition, 2003. xiii + 434, *J. Raman Spectrosc.*, 36, 1012-1012 (DOI: 10.1002/jrs.1407)
- [77]. Edwards H. G. M. (2005), *Modern Raman spectroscopy—a practical approach*. Ewen Smith and Geoffrey Dent. John Wiley and Sons Ltd, Chichester,

2005. Pp. 210. ISBN 0 471 49668 5 (cloth, hb); 0 471 49794 0 (pbk), *J. Raman Spectrosc.*, 36, 835- 835 (DOI: 10.1002/jrs.1320)

[78]. Long D. A. (2004), *Handbook of Raman spectroscopy. From the research laboratory to the process line.* Edited by Ian R. Lewis and Howell G. M. Edwards. Marcel Dekker, New York and Basel, 2001. Price \$225, *J. Raman Spectrosc.*, 35, 91- 91 (DOI: 10.1002/jrs.1117)

[79]. D. F. Swinehart, “The beer-lambert law,” *J. Chem. Educ.*, vol. 39, no. 7, p. 333, 1962.

[80]. L. Yang and B. Kruse, “Revised Kubelka–Munk theory. I. Theory and application,” *JOSA A*, vol. 21, no. 10, pp. 1933–1941, 2004.

[81]. J. Taus, “Amorphous and liquid semiconductor,” *Plenums Press New York Lond.*, vol. 18, 1974.

[82]. S. Hong, E. Kim, D.-W. Kim, T.-H. Sung, and K. No, “On measurement of optical band gap of chromium oxide films containing both amorphous and crystalline phases,” *J. Non-Cryst. Solids*, vol. 221, no. 2–3, pp. 245–254, 1997.

[83]. J. C. Woicik, J. G. Pellegrino, B. Steiner, K. E. Miyano, S. G. Bompadre, L. B. Sorensen, T.-L. Lee, and S. Khalid, *Phys. Rev. Lett.* 79, 5026 (1997).

[84]. J. C. Woicik, C. E. Bouldin, K. E. Miyano, and C. A. King, *Phys. Rev. B* 55, 15386 (1997) [85]. Titas Dutta, P. Gupta, A. Gupta, and J. Narayan *JOURNAL OF APPLIED PHYSICS* 108, 083715 2010

[86]. C. Bagavath · L. Nasi · J. Kumar *Appl. Phys. A* (2017) 123:287

[87]. María Taeño , David Maestre , Julio Ramírez-Castellanos , Shaohui Li , Pooi See Lee 3 and Ana Cremades *Nanomaterials* 2021, 11, 444. <https://doi.org/10.3390/nano11020444>

[88] W. B. Dai, E. H. Song, J. L. Wang and Q. Y. Zhang\**Cryst EngComm*, 2016, 18, 2679 DOI: 10.1039/c6ce00125d

- [89]. Doo-Sik Kim,<sup>a</sup> Jae-Hun Yang,<sup>a</sup> Subramanian Balaji,<sup>b</sup> Hyun-Jung Cho,<sup>a</sup> Min-Kyung Kim,<sup>a</sup> Dong-Uk Kang,<sup>a</sup> Yahia Djaoued<sup>b</sup> and Young-Uk Kwon<sup>\*ac</sup>  
CrystEngComm DOI: 10.1039/b901957j
- [90]. (Ehssan Salah Hassan<sup>1</sup> • Asrar Abdulmunem Saeed<sup>1</sup> • Abdulhussain K. Elttayef<sup>2</sup> J Mater Sci: Mater Electron (2016) 27:1270–1277 DOI 10.1007/s10854-015-3885-3)
- [91]. Biswajit Choudhury , Munmun Dey and Amarjyoti Choudhury Choudhury et al. International Nano Letters 2013
- [92]. Sundar Kunwar, Puran Pandey and Jihoon Lee\* ACS Omega 2019, 4, 17, 17340–17351 doi.org/10.1021/acsomega.9b02066
- [93]. S. Patskovsky; et al. (2014). "Wide-field hyperspectral 3D imaging of functionalized gold nanoparticles targeting cancer cells by reflected light microscopy". Journal of Biophotonics. 8 (5): 1–7. doi:10.1002/jbio.201400025. PMID 24961507.
- [94]. ] Xu, X., Li, H., Hasan, D., Ruoff, R. S., Wang, A. X. and Fan, D. L. (2013), Near-Field Enhanced Plasmonic-Magnetic Bifunctional Nanotubes for Single Cell Bioanalysis. Adv. Funct. Mater. doi:10.1002/adfm.201203822
- [95]. Raguse, John (April 15, 2015). "Correlation of Electroluminescence with Open-Circuit Voltage from Thin-Film CdTe Solar Cells". Journal of Photovoltaics. 5 (4): 1175–1178. doi:10.1109/JPHOTOV.2015.2417761.
- [96]. Dworzak, U. Haboek, A.V. Rodina, Bound exciton, and donor–acceptor pair recombinations in ZnO, Phys. Status Solidi B. 241 (2004) 231–260. doi:10.1002/pssb.200301962.
- [97]. F. Tuomisto, K. Saarinen, D.C. Look, G.C. Farlow, Introduction, and recovery of point defects in electron irradiated ZnO, Phys. Rev. B. 72 (2005) 085206. doi:10.1103/PhysRevB.72.085206.

[98]. ] C.F. Windisch, G.J. Exarhos, C. Yao, and L.-Q. Wang, *Journal of Applied Physics* 101, 123711 (2007). [99]. D.M. Hofmann, D. Pfisterer, J. Sann, B.K. Meyer, R. Tena- Zaera, V. Munoz-Sanjose, T. Frank, and G. Pensl, *Appl. Phys.* A88, 147 (2007).

[100]. Raguse, John (April 15, 2015). "Correlation of Electroluminescence with Open-Circuit Voltage from Thin-Film CdTe Solar Cells". *Journal of Photovoltaics*. 5 (4): 1175–1178. doi:10.1109/JPHOTOV.2015.2417761

[101]. Raguse, John (April 15, 2015). "Correlation of Electroluminescence with Open-Circuit Voltage from Thin-Film CdTe Solar Cells". *Journal of Photovoltaics*. 5 (4): 1175–1178. doi:10.1109/JPHOTOV.2015.2417761.

[102]. 26 S. Schuppler, S. L. Friedman, M. A. Marcus et al., "Dimensions of luminescent oxidized and porous silicon structures," *Physical Review Letters*, vol. 72, no. 16, pp. 2648–2651, 1994.

[103]. F. Severiano, G. García, L. Castañeda, J. M. Gracia-Jiménez, Heberto Gómez-Pozos,<sup>4</sup> and J. A. Luna-López<sup>2</sup> *Journal of Nanomaterials* Volume 2014, Article ID 409493, 7 pages <http://dx.doi.org/10.1155/2014/409493>

[104]. Z.J. Jiang, G.D. Tang, and J. Dai, *Chinese J. Spectr. Lab.* 19, 593 (2002). Y.S. Chang, Y.H. Chang, I.G. Chen, G.J. Chen, and Y.L. Chai, *J. Crystal Growth* 243, 319 (2002).

[105]. LOKESH BUDIG<sup>1a</sup> , MADHUSUDHANA RAO NASINA<sup>a</sup> , KALEEMULLA SHAIK<sup>a</sup> and SIVAKUMAR AMARAVADI<sup>b</sup> *J. Chem. Sci.* Vol. 127, No. pp. 509–518(2015).

[106]. Ximena Jaramillo-Fierro <sup>1,2,\*</sup> , Silvia González <sup>2</sup> , Hipatia Alvarado Jaramillo <sup>2</sup>, and Francesc Medina <sup>1</sup> *Nanomaterials* 2020, 10, 1891.

- [107]. LOKESH BUDIGI<sup>a</sup> , MADHUSUDHANA RAO NASINA<sup>a</sup> , KALEEMULLA SHAIK<sup>a</sup> and SIVAKUMAR AMARAVADI<sup>b</sup> J. Chem. Sci. Vol. 127, No. pp. 509–518(2015).
- [108]. Zahid Ali <sup>a,n</sup> , Sajad Ali <sup>a,b</sup> , Iftikhar Ahmad <sup>a</sup> , Imad Khan <sup>a</sup> , H.A. Rahnamaye Aliabad <sup>c</sup> Z. Ali et al. / Physica B 420 (2013) 54–57
- [109]. Xinyi Li <sup>a,b</sup> , Yunlan Wang <sup>a,b</sup> , Weifeng Liu <sup>a,b,n</sup> , Guoshun Jiang <sup>a,b</sup> , Changfei Zhu <sup>a,b,n</sup> X. Li et al. / Materials Letters 85 (2012) 25–28.
- [110]. R.S. Raveendra<sup>a,b</sup>, P.A. Prashantha,<sup>\*</sup>, R. Hari Krishnac,<sup>\*</sup>, N.P. Bhagya<sup>a</sup>, B.M. Nagabhushanac, H. Raja Naika <sup>d</sup>, K. Lingarajud, H. Nagabhushana <sup>e</sup>, B. Daruka Prasad<sup>f</sup> R.S. Raveendra et al. / Journal of Asian Ceramic Societies 2 (2014) 357–365.
- [111]. Ying Liu,<sup>ab</sup> Dapeng Xu, <sup>a</sup> Tian Cui, <sup>a</sup> Huamin Yu,<sup>ac</sup> Xianfeng Lia and Liang L 26436 | RSC Adv., 2019, 9, 26436–26441.
- [112]. J. Ruiz-Fuertes,<sup>1,\*</sup> B. Winkler,<sup>1</sup> T. Bernert,<sup>2</sup> L. Bayarjargal,<sup>1</sup> W. Morgenroth,<sup>1</sup> M. Koch-Muller, <sup>3</sup> K. Refson,<sup>4</sup> V. Milman,<sup>5</sup> and N. Tamura PHYSICAL REVIEW B 91, 214110 (2015).
- [113]. Tauc, J., Menth, A., 1972 Non Cryst. Solids 569 8
- [114]. J.W. Jeon, D.W. Jeon, T. Sahoo, M. Kim, J.H. Baek, J. L. Hoffman, N. S. Kim and I.H. Lee, Effect of Annealing Temperature on Optical Band-Gap of Amorphous Indium Zinc Oxide Film, Journal of Alloys and Compounds, 509 (41), (2011) 10062 - 10065.
- [115]. Keigo Suzuki, And Kazunori Kijima. 2005. Optical Band Gap Of Barium Titanate Nanoparticles Prepared By Plasma Chemical Vapor Deposition, Japanese Journal of Applied Physics, Vol. 44, No. 4a, 2005, Pp. 2081–2082, The Japan Society of Applied Physics.
- [116]. Zahid Ali <sup>a,n</sup> , Sajad Ali <sup>a,b</sup> , Iftikhar Ahmad <sup>a</sup> , Imad Khan <sup>a</sup> , H.A. Rahnamaye Aliabad <sup>c</sup> Z. Ali et al. / Physica B 420 (2013) 54–57.

[117]. . Zahid Ali a,n , Sajad Ali a,b , Iftikhar Ahmad a , Imad Khan a , H.A. Rahnamaye Aliabad c Z. Ali et al. / Physica B 420 (2013) 54–57.

[118]. Nepal N., Li J., Nakarmi M. L., Lin J. Y., Jianga H. X., Temperature and compositional dependence of the energy band gap of AlGaIn alloys, Department of Physics, Kansas State University, Manhattan, Kansas 66506-260

